A&A 536, A24 (2011)
DOI: 10.1051/0004-6361/201116485

Astronomy & Astrophysics
Special feature

Planck early results

Planck early results. XXIV. Dust in the diffuse interstellar medium and the Galactic halo⋆

Planck Collaboration: A. Abergel[46], P. A. R. Ade[71], N. Aghanim[46], M. Arnaud[57], M. Ashdown[55,4], J. Aumont[46], C. Baccigalupi[69], A. Balbi[28], A. J. Banday[75,7,62], R. B. Barreiro[52], J. G. Bartlett[3,53], E. Battaner[77], K. Benabed[47], A. Benoît[45], J.-P. Bernard[75,7], M. Bersanelli[25,40], R. Bhatia[5], K. Blagrave[6], J. J. Bock[53,8], A. Bonaldi[36], J. R. Bond[6], J. Borrill[61,72], F. R. Bouchet[47], F. Boulanger[46], M. Bucher[3], C. Burigana[39], P. Cabella[28], C. M. Cantalupo[61], J.-F. Cardoso[58,3,47], A. Catalano[3,56], L. Cayón[18], A. Challinor[49,55,9], A. Chamballu[43], L.-Y Chiang[48], C. Chiang[17], P. R. Christensen[66,29], D. L. Clements[43], S. Colombi[47], F. Couchot[60], A. Coulais[56], B. P. Crill[53,67], F. Cuttaia[39], L. Danese[69], R. D. Davies[54], R. J. Davis[54], P. de Bernardis[24], G. de Gasperis[28], A. de Rosa[39], G. de Zotti[36,69], J. Delabrouille[3], J.-M. Delouis[47], F.-X. Désert[42], C. Dickinson[54], S. Donzelli[40,50], O. Doré[53,8], U. Dörl[62], M. Douspis[46], X. Dupac[32], G. Efstathiou[49], T. A. Enßlin[62], H. K. Eriksen[50], F. Finelli[39], O. Forni[75,7], M. Frailis[38], E. Franceschi[39], S. Galeotta[38], K. Ganga[3,44], M. Giard[75,7], G. Giardino[33], Y. Giraud-Héraud[3], J. González-Nuevo[69], K. M. Górski[53,79], S. Gratton[55,49], A. Gregorio[26], A. Gruppuso[39], F. K. Hansen[50], D. Harrison[49,55], G. Helou[8], S. Henrot-Versillé[60], D. Herranz[52], S. R. Hildebrandt[8,59,51], E. Hivon[47], M. Hobson[4], W. A. Holmes[53], W. Hovest[62], R. J. Hoyland[51], K. M. Huffenberger[78], A. H. Jaffe[43], G. Joncas[12], A. Jones[46], W. C. Jones[17], M. Juvela[16], E. Keihänen[16], R. Keskitalo[53,16], T. S. Kisner[61], R. Kneissl[31,5], L. Knox[20], H. Kurki-Suonio[16,34], G. Lagache[46], J.-M. Lamarre[56], A. Lasenby[4,55], R. J. Laureijs[33], C. R. Lawrence[53], S. Leach[69], R. Leonardi[32,33,21], C. Leroy[46,75,7], M. Linden-Vørnle[11], F. J. Lockman[64], M. López-Caniego[52], P. M. Lubin[21], J. F. Macías-Pérez[59], C. J. MacTavish[55], B. Maffei[54], D. Maino[25,40], N. Mandolesi[39], R. Mann[70], M. Maris[38], D. J. Marshall[75,7], P. Martin[6], E. Martínez-González[52], S. Masi[24], S. Matarrese[23], F. Matthai[62], P. Mazzotta[28], P. McGehee[44], P. R. Meinhold[21], A. Melchiorri[24], L. Mendes[32], A. Mennella[25,38], M.-A. Miville-Deschênes[46,6], A. Moneti[47], L. Montier[75,7], G. Morgante[39], D. Mortlock[43], D. Munshi[71,49], A. Murphy[65], P. Naselsky[66,29], F. Nati[24], P. Natoli[27,2,39], C. B. Netterfield[14], H. U. Nørgaard-Nielsen[11], F. Noviello[46], D. Novikov[43], I. Novikov[66], I. J. O'Dwyer[53], S. Osborne[74], F. Pajot[46], R. Paladini[73,8], F. Pasian[38], G. Patanchon[3], O. Perdereau[60], L. Perotto[59], F. Perrotta[69], F. Piacentini[24], M. Piat[3], D. Pinheiro Gonçalves[14], S. Plaszczynski[60], E. Pointecouteau[75,7], G. Polenta[2,37], N. Ponthieu[46], T. Poutanen[34,16,1], G. Prézeau[8,53], S. Prunet[47], J.-L. Puget[46], J. P. Rachen[62], W. T. Reach[76], M. Reinecke[62], C. Renault[59], S. Ricciardi[39], T. Riller[62], I. Ristorcelli[75,7], G. Rocha[53,8], C. Rosset[3], M. Rowan-Robinson[43], J. A. Rubiño-Martín[51,30], B. Rusholme[44], M. Sandri[39], D. Santos[59], G. Savini[68], D. Scott[15], M. D. Seiffert[53,8], P. Shellard[9], G. F. Smoot[19,61,3], J.-L. Starck[57,10], F. Stivoli[41], V. Stolyarov[4], R. Stompor[3], R. Sudiwala[71], J.-F. Sygnet[47], J. A. Tauber[33], L. Terenzi[39], L. Toffolatti[13], M. Tomasi[25,40], J.-P. Torre[46], M. Tristram[60], J. Tuovinen[63], G. Umana[35], L. Valenziano[39], P. Vielva[52], F. Villa[39], N. Vittorio[28], L. A. Wade[53], B. D. Wandelt[47,22], A. Wilkinson[54], D. Yvon[10], A. Zacchei[38], and A. Zonca[21]

(Affiliations can be found after the references)

Received 9 January 2011 / Accepted 22 September 2011

ABSTRACT

This paper presents the first results from a comparison of *Planck* dust maps at 353, 545 and 857 GHz, along with IRAS data at 3000 (100 μm) and 5000 GHz (60 μm), with Green Bank Telescope 21-cm observations of H I in 14 fields covering more than 800 deg^2 at high Galactic latitude. The main goal of this study is to estimate the far-infrared to sub-millimeter (submm) emissivity of dust in the diffuse local interstellar medium (ISM) and in the intermediate-velocity (IVC) and high-velocity clouds (HVC) of the Galactic halo. Galactic dust emission for fields with average H I column density lower than 2×10^{20} cm^{-2} is well correlated with 21-cm emission because in such diffuse areas the hydrogen is predominantly in the neutral atomic phase. The residual emission in these fields, once the H I-correlated emission is removed, is consistent with the expected statistical properties of the cosmic infrared background fluctuations. The brighter fields in our sample, with an average H I column density greater than 2×10^{20} cm^{-2}, show significant excess dust emission compared to the H I column density. Regions of excess lie in organized structures that suggest the presence of hydrogen in molecular form, though they are not always correlated with CO emission. In the higher H I column density fields the excess emission at 857 GHz is about 40% of that coming from the H I, but over all the high latitude fields surveyed the molecular mass faction is about 10%. Dust emission from IVCs is detected with high significance by this correlation analysis. Its spectral properties are consistent with, compared to the local ISM values, significantly hotter dust ($T \sim 20$ K), lower submm dust opacity normalized per H-atom, and a relative abundance of very small grains to large grains about four times higher. These results are compatible with expectations for clouds that are part of the Galactic fountain in which there is dust shattering and fragmentation. Correlated dust emission in HVCs is not detected; the average of the 99.9% confidence upper limits to the emissivity is 0.15 times the local ISM value at 857 and 3000 GHz, in accordance with gas phase evidence for lower metallicity and depletion in these clouds. Unexpected anti-correlated variations of the dust temperature and emission cross-section per H atom are identified in the local ISM and IVCs, a trend that continues into molecular environments. This suggests that dust growth through aggregation, seen in molecular clouds, is active much earlier in the cloud condensation and star formation processes.

Key words. infrared: ISM – methods: data analysis – dust, extinction – submillimeter: ISM – Galaxy: halo – local insterstellar matter

⋆ Corresponding author: M.-A. Miville-Deschênes,
e-mail: mamd@ias.u-psud.fr

1. Introduction

Planck[1] (Tauber et al. 2010; Planck Collaboration 2011a) is the third-generation space mission to measure the anisotropy of the cosmic microwave background (CMB). It observes the sky in nine frequency bands covering 30–857 GHz with high sensitivity and angular resolution from 31′ to 5′. The Low Frequency Instrument (LFI; Mandolesi et al. 2010; Bersanelli et al. 2010; Mennella et al. 2011) covers the 30, 44, and 70 GHz bands with amplifiers cooled to 20 K. The High Frequency Instrument (HFI; Lamarre et al. 2010; Planck HFI Core Team 2011a) covers the 100, 143, 217, 353, 545, and 857 GHz bands with bolometers cooled to 0.1 K. *Planck*'s sensitivity, angular resolution, and frequency coverage make it a powerful instrument for Galactic and extragalactic astrophysics as well as cosmology. This paper presents the first results of the analysis of *Planck* observations of the diffuse interstellar medium (ISM) at high Galactic latitude.

From the pioneering work of Spitzer and Field (Spitzer 1956; Field 1965; Field et al. 1969), observations of the diffuse ISM including intermediate and high-velocity clouds (IVCs and HVCs) have been the basis of our understanding of the dynamical interplay between ISM phases and the disk-halo connection in relation to star formation. Space-based observations have given us spectacular perspectives on the diffuse Galactic infrared emission, which highlight the role of dust not only as a tracer of the diffuse ISM but also as an agent in its evolution.

The InfraRed Astronomical Satellite (IRAS) revealed the intricate morphology of infrared cirrus (Low et al. 1984) and prompted a wide range of observations. The cirrus is inferred to be inhomogeneous turbulent dusty clouds with dense CO-emitting gas intermixed with cold (CNM) and warm (WNM) neutral atomic gas and also diffuse H_2. From imaging by the *Spitzer* Space Telescope, and very recently by the *Herschel* Space Observatory, their structure is now known to extend to much smaller angular scales than observable at the IRAS resolution (Ingalls et al. 2004; Martin et al. 2010; Miville-Deschênes et al. 2010). Observations from IRAS, the Infrared Space Observatory (ISO), and *Spitzer* have also been used to characterize changes in the spectral energy distribution (SED) from mid- to far-IR wavelengths, which have been interpreted as evidence for variations in the abundance of small stochastically-heated dust particles. The correlation with H I spectroscopic data suggests that interstellar turbulence may play a role in changing the dust size distribution (Miville-Deschênes et al. 2002a).

Since the breakthrough discoveries made with the COsmic Background Explorer (COBE), the study of dust and the diffuse ISM structure has also become an integral part of the analysis of the CMB and the cosmic infrared extragalactic background (CIB). Our ability to model the spatial and spectral distribution of the infrared cirrus emission could limit our ability to achieve the cosmological goals of *Planck*, as well as of present balloon-borne and ground-based CMB experiments.

Accordingly, the *Planck* survey was designed to provide an unprecedented view of the structure of the diffuse ISM and its dust content. *Planck* extends to sub-millimeter (submm) wavelengths the detailed mapping of the infrared cirrus by the IRAS survey. Its sensitivity to faint Galactic cirrus emission is limited only by the astrophysical noise associated with the anisotropy of the CIB. The *Planck* survey is a major step forward from IRAS for two main reasons. First, by extending the spectral coverage to submm wavelengths, *Planck* allows us to probe the full SED of thermal emission from the large dust grains that are the bulk of the dust mass. Second, the dust temperatures obtained via submm SEDs also help us to disentangle the effects of dust column density, dust heating and dust emission cross-section on the brightness of the dust emission.

The scientific motivation of this paper is to trace the structure of the diffuse ISM, including its elusive diffuse H_2 component, H^+ components, and the evolution of interstellar dust grains within the local ISM and the Galactic halo. We analyze the *Planck* data in selected fields which cover the full range of hydrogen column densities from high Galactic latitude cirrus, observed away from dark molecular clouds such as, e.g., Taurus (Planck Collaboration 2011u). For all of our fields, we have deep 21-cm spectroscopic observations obtained with the Green Bank Telescope (GBT). Our data analysis makes use of, and explores, the dust/gas correlation by spatially correlating *Planck* and IRAS data with H I observations. More specifically our study extends previous work on the diffuse ISM SED carried out with 7° resolution Far InfraRed Absolute Spectrophotometer (FIRAS) data (Boulanger et al. 1996) or with 5′ resolution 100 μm IRAS data (Reach et al. 1998).

The paper is organized as follows. In Sect. 2 we describe the 21-cm data and the construction of the column density map for each H I component. In Sect. 3 we describe the *Planck* and IRAS data. Section 4 describes the main analysis of the paper: the determination of the H I emissivities from 353 to 5000 GHz (60 to 850 μm). Results are presented in Sect. 5 followed by a discussion of some implications in Sect. 6. Conclusions wrap up the paper in Sect. 7.

2. 21-cm data

2.1. The Green Bank Telescope cirrus survey

The 21-cm H I spectra exploited here were obtained with the 100-meter GBT over the period 2005 to 2010, as part of a high-latitude survey of 14 fields (for details, see Martin et al., in prep). The total area mapped is about 825 deg^2. The adopted names, central coordinates, and sizes of the 14 GBT fields are given in Table 1. The brighter fields of the sample, the ones that cover the range of column densities that spans the H I-H_2 transition, are located in the North Celestial Loop region, covering the Polaris flare (POL and POLNOR), the Ursa Major cirrus (UMA and UMAEAST), the bridge between the two (SPIDER) and the interior of the loop (SPC). The largest field in our sample (NEP) is centered on the north ecliptic pole, a region of high coverage for *Planck*. Two fields were targeted for their specific IVC (DRACO and G86). The faintest fields of the sample were selected either because the HVC has a major contribution to the total hydrogen column density (AG, MC, SP) or because they are known CIB targets (N1 and BOOTES).

The spectra were taken with on-the-fly mapping. The primary beam of the GBT at 21-cm has a full-width half-maximum (FWHM) of 9.1′, and so the integration time (4 s) and telescope scan rate were chosen to sample every 3.5′, more finely than the Nyquist interval, 3.86′. The beam is only slightly broadened to 9.4′ in the in-scan direction. Scans were made moving the telescope in one direction (Galactic longitude or Right Ascension), with steps of 3.5′ in the orthogonal coordinate direction before the subsequent reverse scan.

[1] *Planck* (http://www.esa.int/Planck) is a project of the European Space Agency (ESA) with instruments provided by two scientific consortia funded by ESA member states (in particular the lead countries France and Italy), with contributions from NASA (USA) and telescope reflectors provided by a collaboration between ESA and a scientific consortium led and funded by Denmark.

Table 1. The H I fields.

Field	l (deg)	b (deg)	Area (deg^2)	LVC $\langle N_{\rm HI}\rangle$ (10^{19} cm^{-2})	LVC v (km s^{-1})	IVC $\langle N_{\rm HI}\rangle$ (10^{19} cm^{-2})	IVC v (km s^{-1})	HVC $\langle N_{\rm HI}\rangle$ (10^{19} cm^{-2})	HVC v (km s^{-1})
AG	164.8	65.5	26.4	5.3 ± 0.3	−18.7 ± 9.7	9.45 ± 0.19	−51.3 ± 11.4	3.8 ± 0.3	−107.2 ± 17.8
BOOTES	58.0	68.6	49.1	6.93 ± 0.12	−5.2 ± 7.8	3.88 ± 0.13	−34.6 ± 11.9	0.16 ± 0.11	−87.5 ± 10.3
DRACO	92.3	38.5	26.4	6.79 ± 0.12	−1.3 ± 4.6	11.5 ± 0.2	−24.1 ± 8.9	3.4 ± 0.3	−141.8 ± 27.0
G86	88.0	59.1	26.4	8.81 ± 0.13	−0.1 ± 6.5	10.25 ± 0.17	−35.3 ± 9.6	0.36 ± 0.15	−93.7 ± 17.8
MC	56.6	−81.5	30.7	8.4 ± 0.2	−0.7 ± 4.8	5.22 ± 0.13	−18.3 ± 7.1	6.2 ± 0.4	−106.5 ± 26.3
N1	85.3	44.3	26.4	6.4 ± 0.2	4.3 ± 10.1	2.84 ± 0.19	−23.1 ± 7.2	3.0 ± 0.3	−112.8 ± 16.9
NEP	96.4	30.0	146.5	26.16 ± 0.19	−2.2 ± 11.3	14.41 ± 0.18	−42.0 ± 14.1	1.10 ± 0.16	−108.4 ± 11.6
POL	124.9	27.5	60.6	62.6 ± 0.5	−7.3 ± 15.0	5.0 ± 0.3	−69.2 ± 12.6	—	—
POLNOR	125.0	37.4	60.6	39.4 ± 0.4	−2.4 ± 17.3	3.4 ± 0.2	−63.2 ± 9.7	—	—
SP	132.3	47.5	26.4	6.1 ± 0.2	−2.7 ± 10.8	3.8 ± 0.2	−51.8 ± 11.3	1.8 ± 0.2	−138.5 ± 11.9
SPC	135.6	29.3	102.1	30.3 ± 0.4	−8.3 ± 15.2	2.7 ± 0.2	−62.0 ± 8.2	0.9 ± 0.2	−186.4 ± 14.8
SPIDER	134.9	40.0	103.8	18.5 ± 0.2	6.0 ± 7.1	8.4 ± 0.3	−39.3 ± 18.7	0.27 ± 0.18	−121.7 ± 20.3
UMA	144.2	38.5	80.7	27.9 ± 0.3	3.5 ± 7.9	9.1 ± 0.3	−49.4 ± 12.0	0.9 ± 0.3	−153.3 ± 12.1
UMAEAST	155.7	37.0	61.3	31.7 ± 0.3	0.3 ± 6.4	9.5 ± 0.3	−48.5 ± 13.2	2.9 ± 0.4	−171.8 ± 12.3

Notes. Columns 2–4 give the central Galactic coordinates and size of each field. Columns 5–10 give the average H I column density and its uncertainty (see Appendix A), and the average LSR velocity and HWHM for each H I component.

Data were recorded with the GBT spectrometer by in-band frequency switching, yielding spectra with a local standard of rest (LSR) velocity coverage $-450 \le v_{\rm LSR} \le +355$ km s^{-1} at a resolution of 0.80 km s^{-1}. Spectra were calibrated, corrected for stray radiation, and placed on a brightness temperature ($T_{\rm b}$) scale as described in Blagrave et al. (2010); Boothroyd et al. (2011). A third-order polynomial was fit to the emission-free regions of the spectra to remove any residual instrumental baseline. The spectra were gridded on the equiareal SFL (Sanson-Flamsteed – Calabretta & Greisen 2002) projection to produce a data cube. Some regions were mapped two or three times.

With the broad spectral coverage, all H I components from local gas to HVCs are accessible. The total column density $N_{\rm HI}$ ranges from 0.6×10^{20} cm^{-2} in the SP field to 10×10^{20} cm^{-2} in POL and NEP; the average column density per field ranges from 1.1×10^{20} cm^{-2} in BOOTES to 6.3×10^{20} cm^{-2} in POL.

2.2. The H I components

We use channel maps from the 21-cm GBT spectra to produce maps of the H I column density in different velocity ranges. For convenience we have separated the emission into three components for each field: Low-velocity cloud (LVC), IVC, and HVC. The selection of the velocity range for each component is based on inspection of both the median 21-cm spectrum and the spectrum made from the standard deviation of each channel map. An example of these two spectra for the N1 field is shown in Fig. 1. The dashed and solid lines show the median and standard deviation of the brightness temperature as a function of velocity. The standard-deviation spectrum, more sensitive to the structure within channel maps, is used here to establish the velocity range of the three components in cases where velocity components are blended in the median spectrum. The three shaded backgrounds in Fig. 1 show the velocity ranges used to calculate the H I column density of the three components in this field.

The brightness temperature of each velocity channel was converted to column density, assuming an opacity correction for H I gas with a constant spin temperature $T_{\rm s}$, to provide an estimate of the total H I column density of each component:

$$N_{\rm HI}(x,y) = A \times T_{\rm s} \sum_{v} -\ln\left(1 - \frac{T_{\rm b}(x,y,v)}{T_{\rm s}}\right) \Delta v, \quad (1)$$

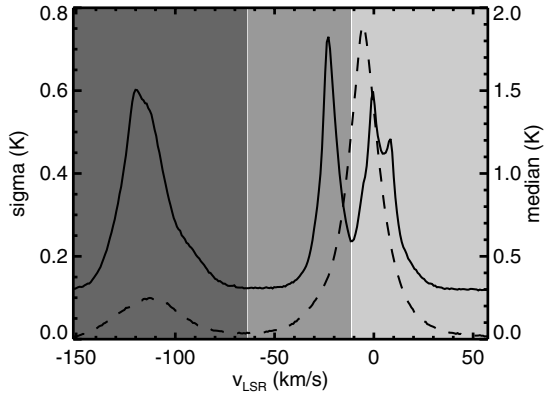

Fig. 1. The median 21-cm spectrum (dashed) and the standard-deviation spectrum (solid) of the N1 field; the shaded backgrounds show the LSR velocity ranges used to estimate LVC, IVC and HVC components (from light to dark grey).

where $A = 1.823 \times 10^{18}$ cm^{-2} (K km s^{-1})$^{-1}$. In the optically-thin case (assuming $T_{\rm s} \gg T_{\rm b}$) this reduces to $N_{\rm HI}(x,y) = A \sum_v T_{\rm b}(x,y,v)\,\Delta v$.

We used $T_{\rm s} = 80$ K which is compatible with the collisional temperature found from the H_2 observations for column densities near 10^{20} cm^{-2} (Gillmon et al. 2006; Wakker 2006). It is also similar to the average H I spin temperature (column density weighted) found by Heiles & Troland (2003). $T_{\rm s}$ will be higher for the WNM, but for these high latitude diffuse lines of sight $T_{\rm b} \ll 80$ K for the broad WNM lines, and so adopting the wrong $T_{\rm s}$ is of no consequence. For most fields the correction is less than 3% compared to the optically-thin assumption. Indeed very few of our 21-cm spectra reach brightness temperatures above 40 K – only 3% of the spectra in POL field, the brightest one in the sample. For these "extreme" cases the opacity correction to the column density reaches 35%. Figures 2 and 3 show the H I column density maps of all fields, in units of 10^{20} cm^{-2}.

2.3. Uncertainties in $N_{\rm HI}$

The main analysis presented here relies on a correlation analysis between far-infrared/submm brightness and $N_{\rm HI}$ of the components deduced from 21-cm emission. In order to estimate

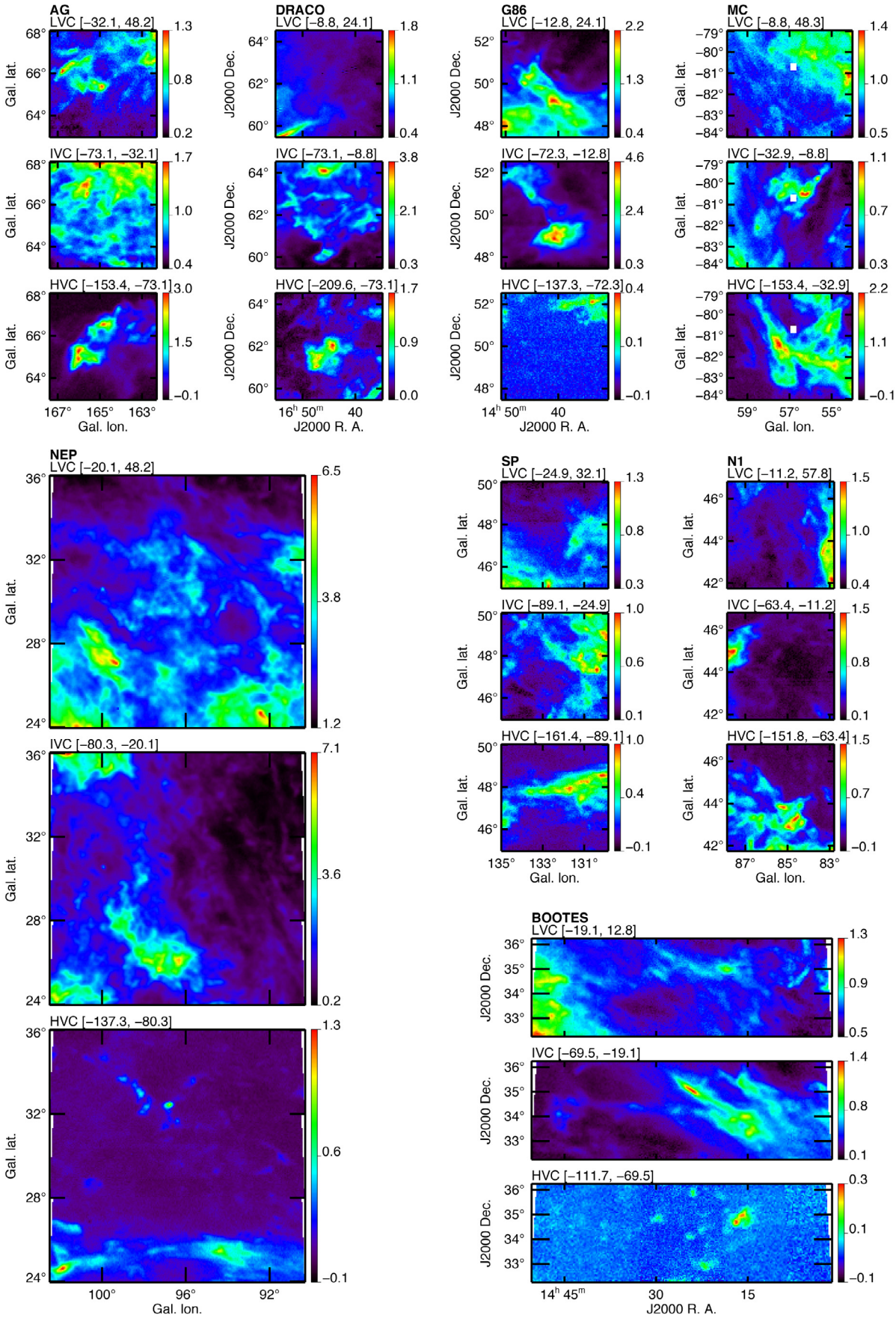

Fig. 2. H I column density maps in units of 10^{20} cm^{-2} for the AG, DRACO, G86, MC, NEP, SP, N1 and BOOTES fields. To show the full detail, the range is different for each H I component for a given field. The LSR velocity range used to compute each H I component map is given in brackets (unit is km s^{-1}).

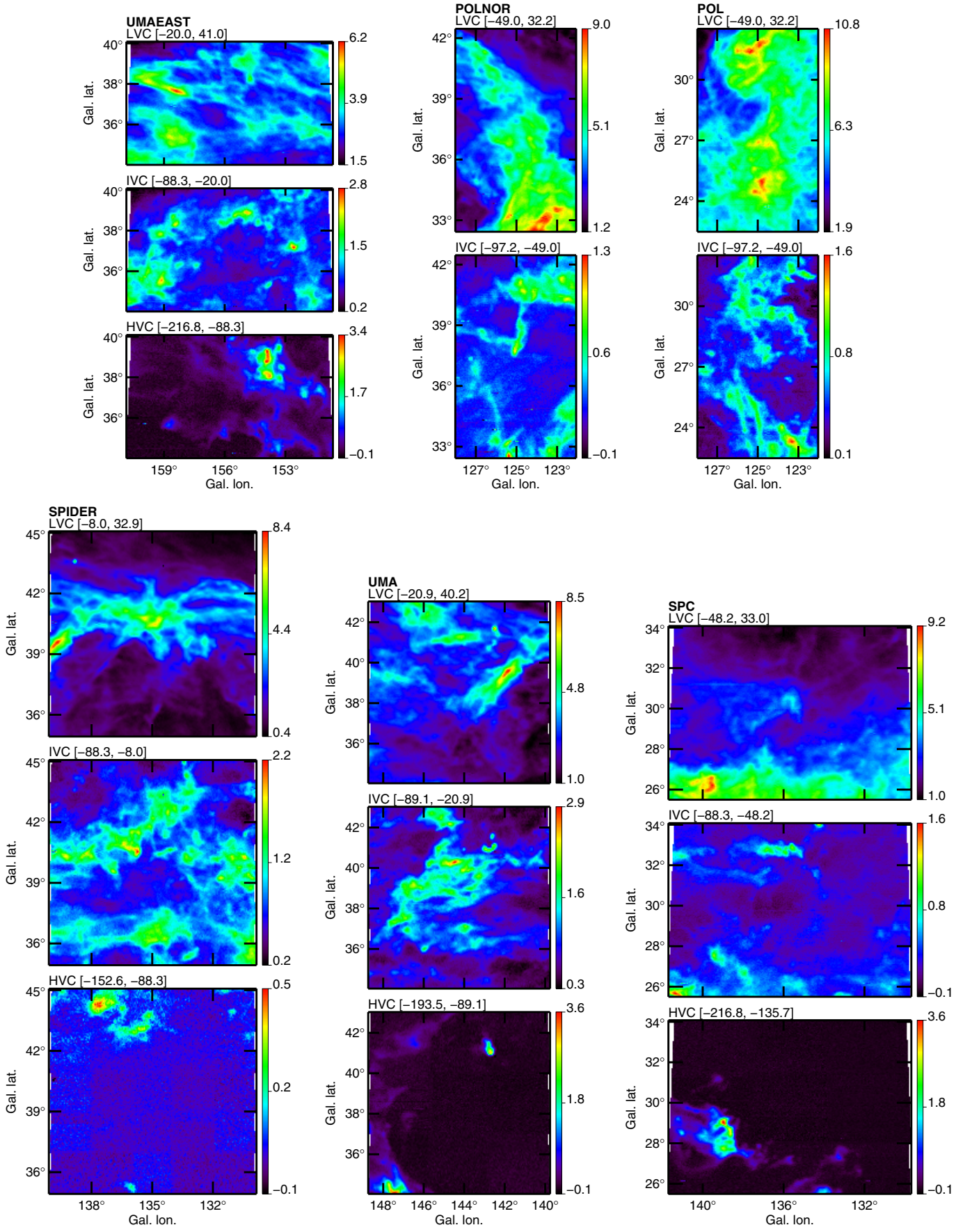

Fig. 3. Like Fig. 2 for fields UMAEAST, POLNOR, POL, SPIDER, UMA and SPC. The M81-M82 complex can be seen in the UMA field near $l = 142.5°$, $b = 41.0°$ in the three H I components. It was masked in the analysis (see Fig. 13).

properly the uncertainties of the deduced correlation coefficients, we need to evaluate the uncertainty of the values of $N_{\rm HI}$ for the H I components. The method described in Appendix A takes advantage of the fact that the GBT observations were obtained in two polarisations. The difference between these spectra gives a direct estimate of the uncertainty in each channel, which can be integrated over the appropriate velocity ranges, providing a column density uncertainty for each H I component. The average H I column densities and uncertainties, expressed in units of 10^{20} cm^{-2}, are given in Table 1 for the three H I components of each field. This table gives also the average velocity of each H I component and an estimate of the half-width at half-maximum of the 21-cm feature.

3. *Planck* and IRAS

3.1. Map construction

Our analysis uses infrared to submm data at 3000 and 5000 GHz (100 and 60 μm, respectively) from IRAS (IRIS, Miville-Deschênes & Lagache 2005) and at 353, 545, and 857 GHz (850, 550, and 350 μm, respectively) from *Planck* (DR2 release; Planck HFI Core Team 2011b), beginning with maps in Healpix form (Górski et al. 2005) with $N_{\rm side}$ = 2048 (pixel size of 1.7′). We concentrated here on the three highest frequencies of *Planck* to avoid the significant contamination from residual CMB fluctuations and interstellar emission other than thermal dust (CO, synchrotron, free-free and spinning dust).

To obtain infrared-submm maps corresponding to each GBT field we first projected each Healpix map, using the nearest neighbour method, onto SFL grids with a pixel size of 1.7′. Each grid was centred on a given GBT field with a size 10% larger in each direction in order to avoid edge effects in subsequent convolution steps. Each SFL map was then converted to MJy sr^{-1} and point sources were removed and replaced by interpolation of the surrounding map[2]. The map was then convolved to bring it to the GBT 9.4′ resolution and finally projected, using bi-linear interpolation, on the actual GBT grid (3.5′ pixel^{-1}). The *Planck* and IRAS maps for our fields are shown in Figs. 4 to 11. As will be discussed in Sect. 4, these figures also show models of this emission based on H I observations in a masked subset of the map, and the residual map on subtracting this model from the entire field. The residuals are largest for those areas in the map not used to constrain the model.

3.2. Dust brightness uncertainty

To estimate the noise level of the *Planck* and IRAS maps we used the method described in Sect. 5.1 of Miville-Deschênes & Lagache (2005). For both data sets we used the difference of maps of the same region of the sky obtained with different subsamples of the data. These difference maps, properly weighted by their coverage maps, provide an estimate of the statistical properties of the noise. For *Planck* the noise was estimated using the difference of the first and second half ring maps (Planck HFI Core Team 2011b). In the case of IRAS, each ISSA plate is the combination of up to three maps built from independent observations over the life of the satellite. We built difference maps from these three sets of maps. The procedure used to estimate the *Planck* and IRAS noise levels at the GBT resolution is detailed in Appendix B. The noise levels for each field and each frequency are given in Table B.1.

4. Dust–HI correlation

4.1. Model

Many studies, mostly using the IRAS and COBE data compared with various 21-cm surveys (Boulanger & Pérault 1988; Joncas et al. 1992; Jones et al. 1995; Boulanger et al. 1996; Arendt et al. 1998; Reach et al. 1998; Lockman & Condon 2005; Miville-Deschênes et al. 2005), have revealed the strong correlation between far-infrared/submm dust emission and 21-cm integrated emission $W_{\rm HI}$[3] at high Galactic latitudes. In particular Boulanger et al. (1996) studied this relation over the whole high Galactic latitude sky. They reported a tight dust–H I correlation for $W_{\rm HI} < 250$ K km s^{-1}, corresponding to $N_{\rm HI} < 4.6 \times 10^{20}$ cm^{-2}. For higher column densities the dust emission systematically exceeds that expected by extrapolating the correlation. Examining specific high Galactic latitude regions, Arendt et al. (1998) and Reach et al. (1998) found infrared excesses with respect to $N_{\rm HI}$, with a threshold varying from 1.5 to 5.0 $\times$ 10^{20} cm^{-2}.

Part of this excess is due to the effect of 21-cm self-absorption that produces a systematic underestimate of the column density when deduced with the optically thin assumption. Even though this effect is only at a level of a few percent in our case because of the low column densities, applying an opacity correction (see Sect. 2.2) helps to limit this systematic effect.

Most of the infrared/submm excess is usually attributed to dust associated with hydrogen in molecular form. This hypothesis is in accordance with UV absorption measurements that show a sudden increase of the H_2 absorption at $N_{\rm H} = (3-5) \times 10^{20}$ cm^{-2} (Savage et al. 1977; Gillmon et al. 2006), roughly the threshold for departure from the linear correlation between dust emission and $N_{\rm HI}$. It is also observed that the pixels showing evidence of excess are spatially correlated and correspond to, or at least are in the vicinity of, known molecular clouds traced by CO emission. See also the discussion in Sect. 6.1.

A third source of this excess emission could be dust associated with the Warm Ionized Medium (WIM) but detection of this component is difficult (Arendt et al. 1998; Lagache et al. 2000) because there is no direct tracer of the ionized gas column density; Hα depends on the square of the electron density and part of the structure seen in Hα might be back-scattering of diffuse Galactic emission on dust and not photons produced within cirrus clouds (Witt et al. 2010).

Finally, in the most diffuse regions of the high-latitude sky, the fluctuations of the CIB are a significant fraction of the brightness fluctuations in the infrared/submm. With a power spectrum flatter (k^{-1}) than that of the interstellar dust emission (k^{-3}) (Miville-Deschênes et al. 2002b, 2007; Lagache et al. 2007; Planck Collaboration 2011n), the CIB anisotropies contribute mostly at small angular scales, producing statistically homogeneous brightness fluctuations over any observed field, like an instrumental noise. Furthermore, because the CIB is unrelated to interstellar emission, the CIB fluctuations cannot be responsible for the excess of infrared emission seen at moderate to high $N_{\rm HI}$ column density.

In the analysis presented here we go a few steps further than the previous studies by: 1) allowing for different dust emissivities for the local ISM (i.e., LVC), IVC, and HVC components;

[2] For *Planck* channels we removed only point sources identified in the ERCSC (Planck Collaboration 2011c). For IRAS maps we used the source removal method described in Miville-Deschênes & Lagache (2005).

[3] Equivalent to optically-thin H I column density.

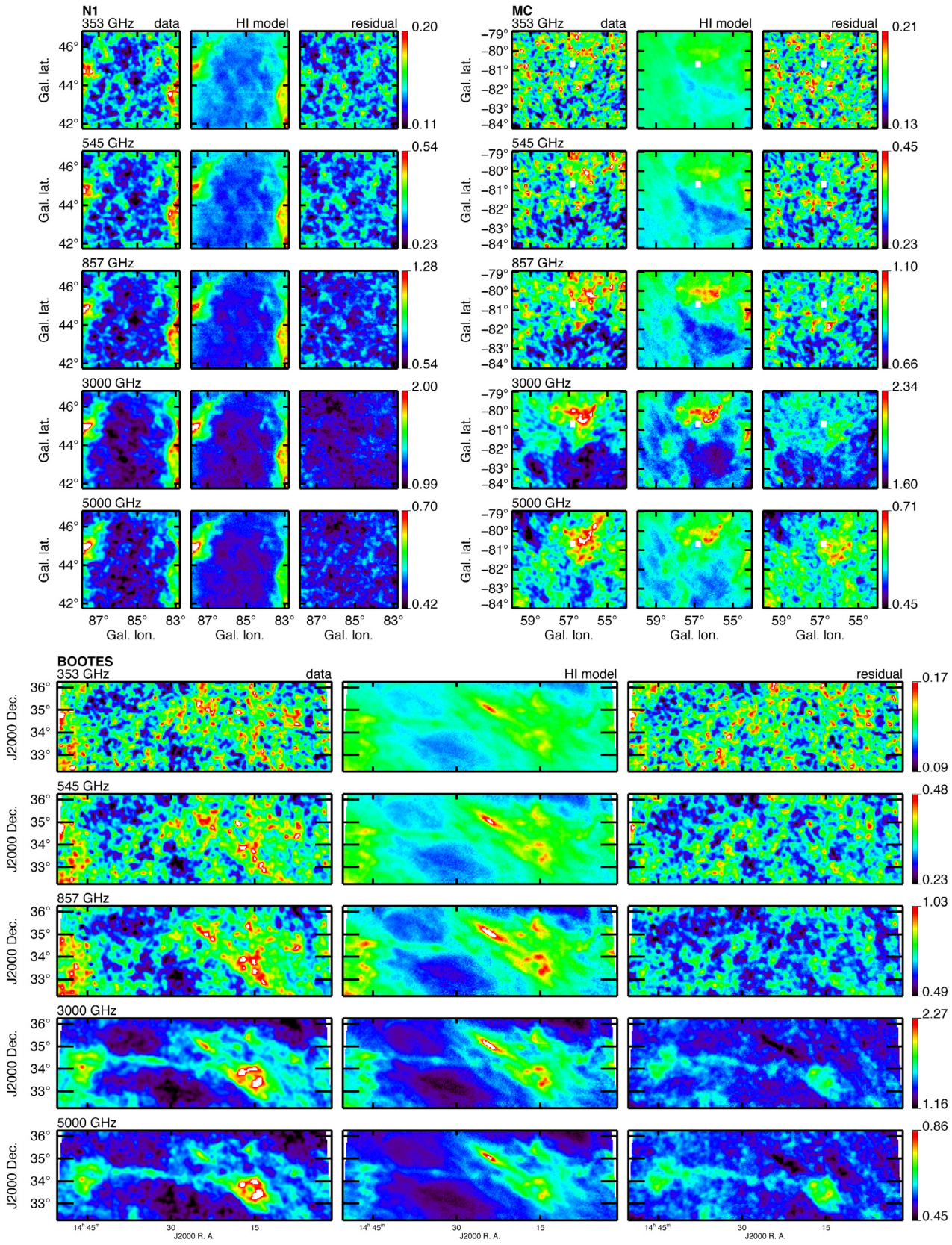

Fig. 4. Dust/gas correlation in N1 (*top-left*), MC (*top-right*) and BOOTES (*bottom*): *Planck* and IRAS raw maps (*left column*), the model of the dust emission based on the H I observations (*middle*: H I *model*, $\sum_{i=1}^{3} \epsilon_{\nu}^{i} N_{\rm HI}^{i}(x, y)$, Eq. (2)) and the residual emission (*right*, see Eq. (6)). Units are MJy sr^{-1}. Data are described in Sect. 3 and model and residual in Sect. 4.

2) applying an opacity correction to the 21-cm brightness temperatures in order to compute a more reliable $N_{\rm HI}$; and 3) taking into account explicitly the CIB fluctuations which turn out to dominate the uncertainties in the derived emissivities.

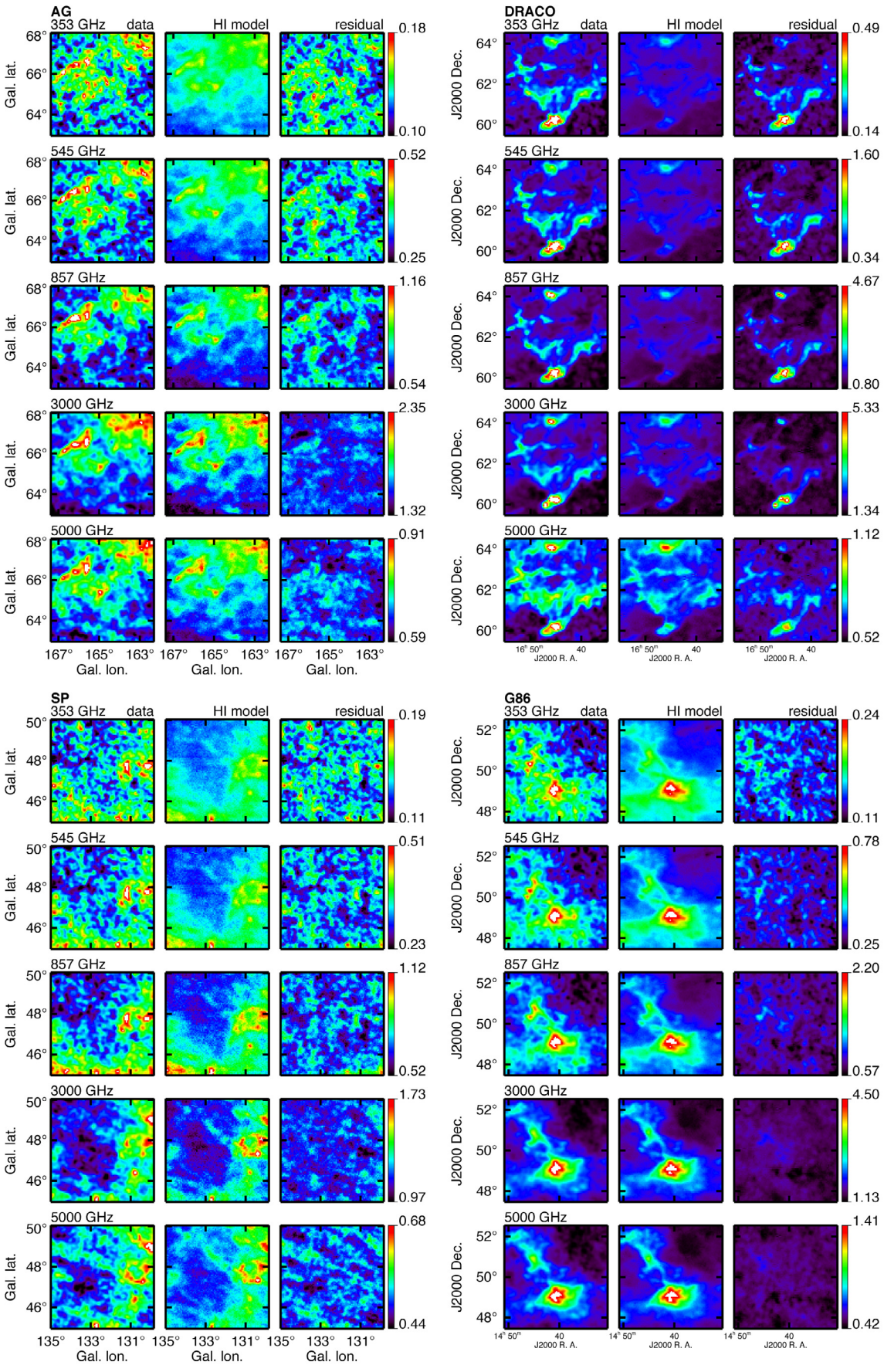

Fig. 5. Like Fig. 4, for AG (*top-left*), DRACO (*top-right*), SP (*bottom-left*) and G86 (*bottom-right*).

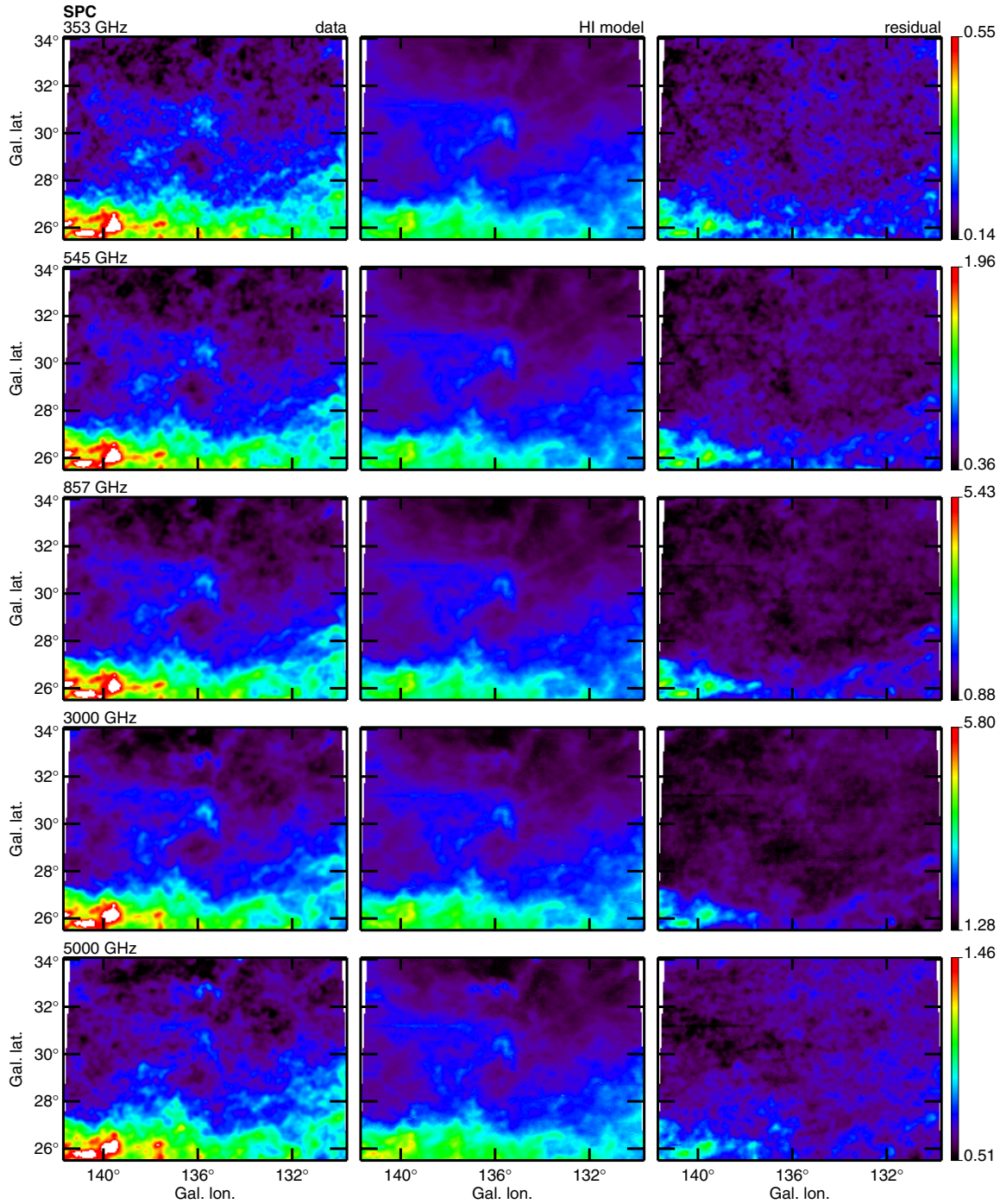

Fig. 6. Like Fig. 4, for field SPC.

In some fields (like G86 with strong IVC emission) the distinctive morphology of the IVC column density map can be seen clearly in the line-of-sight integrated dust emission map (see Figs. 2 and 5 and Martin et al. 1994), but even faint signals can be brought out by formal correlation analysis. We use the following model:

$$I_\nu(x,y) = \sum_{i=1}^{3} \epsilon_\nu^i N_{\rm HI}^i(x,y) + R_\nu(x,y) + Z_\nu, \quad (2)$$

where $I_\nu(x,y)$ is the dust map at frequency ν (IRAS or *Planck*), ϵ_ν^i the emissivity of H I component i (LVC, IVC and HVC), and Z_ν is the zero level of the map. R_ν represents not only the contribution from noise in the data but also any emission in the IRAS and *Planck* bands that is not correlated with $N_{\rm HI}$ including the CIB anisotropies and potential dust emission coming from molecular or ionized gas. In this model we assume that the three HI components $N_{\rm HI}^i(x,y)$ have a constant emissivity ϵ_ν^i over the field. Any spatial variations of the emissivity would also contribute to fluctuations in $R_\nu(x,y)$.

4.2. Estimating the dust emissivities

To estimate the parameters ϵ_ν^i and constant Z_ν we used the IDL function *regress* which, in the case of a general linear least-squares fit, solves the following equation (Press et al. 1995):

$$a = (A^T A)^{-1} \times (A^T b), \quad (3)$$

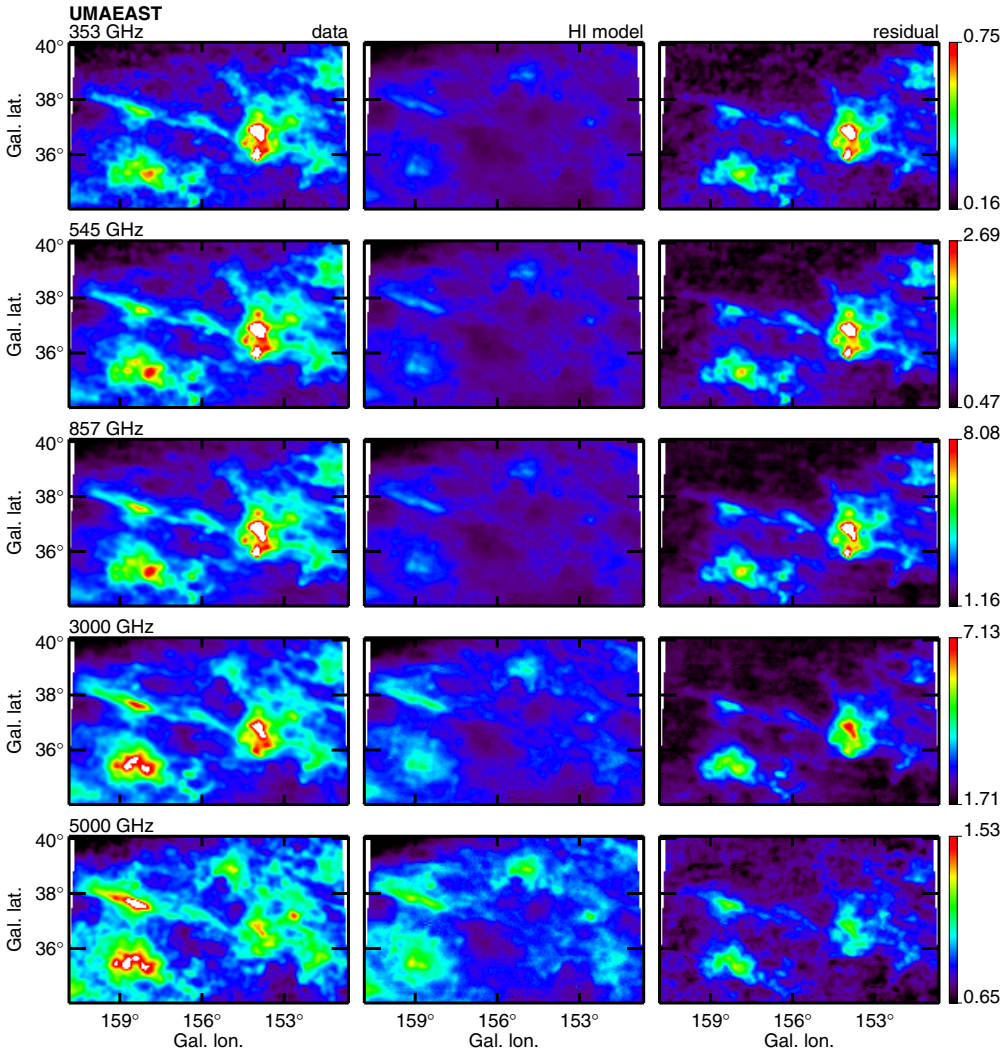

Fig. 7. Like Fig. 4, for field UMAEAST.

where a is the vector of the parameters ϵ_ν^i and b is a vector of the N IRAS or *Planck* data points from the map, divided by their respective error:

$$b_i = \frac{I_\nu(i)}{\sigma_\nu}. \quad (4)$$

A is an $N \times M$ matrix that includes the $N_{\rm HI}$ values of the M H I components,

$$A_{ij} = \frac{N_{\rm HI}^j(i)}{\sigma_\nu}. \quad (5)$$

Regress uses a Gaussian elimination method for the inversion.

For the model described in Eq. (2), the least-squares fit method provides a maximum-likelihood estimation of the parameters ϵ_ν^i provided that the residual term $R_\nu(x, y)$ is uncorrelated with $N_{\rm HI}^i$ and its fluctuations are normally distributed (i.e., white noise). In addition, in order that the parameter estimates not be biased, the uncertainties on $N_{\rm HI}^i$ have to be comparatively small; we will show (see Sect. 4.5) that this last condition is satisfied for our data. On the other hand, we will also show that the residual term $R_\nu(x, y)$ is clearly not compatible with white noise. Even for the most diffuse fields in our sample, where the CIB fluctuations dominate the residual emission and the Probability Density Function (PDF) of $R_\nu(x, y)$ is normally distributed, the condition that there be no (not even chance) correlation with $N_{\rm HI}$ is not satisfied, because the power spectrum of the CIB is not white, but rather like k^{-1} (Planck Collaboration 2011n). For brighter fields, where spatial variation of the dust emission with respect to the H I templates is expected (due to the presence of molecules, a poor H I opacity correction, or spatial variation of dust properties), the residual is not even normally distributed.

To limit the influence of these effects, and in order to focus on estimating the dust emissivity of the H I components, we relied on a masking procedure to flag and remove obvious outliers with respect to the correlation, and on Monte-Carlo simulations to estimate the ϵ_ν^i uncertainties and bias (see Sect. 4.5).

4.3. Masking

In order to limit the effect of lines of sight with significant "excess" dust emission that is not associated with H I gas, most previous authors used only data points with $N_{\rm HI}$ lower than a given threshold to stay in a regime of linear correlation. This thresholding was motivated by the fact that above some $N_{\rm HI}$ the extinction and self-shielding of H_2 are strong enough to limit photodissociation, whereas below the threshold the hydrogen is mostly atomic. The threshold depends sensitively on local gas density

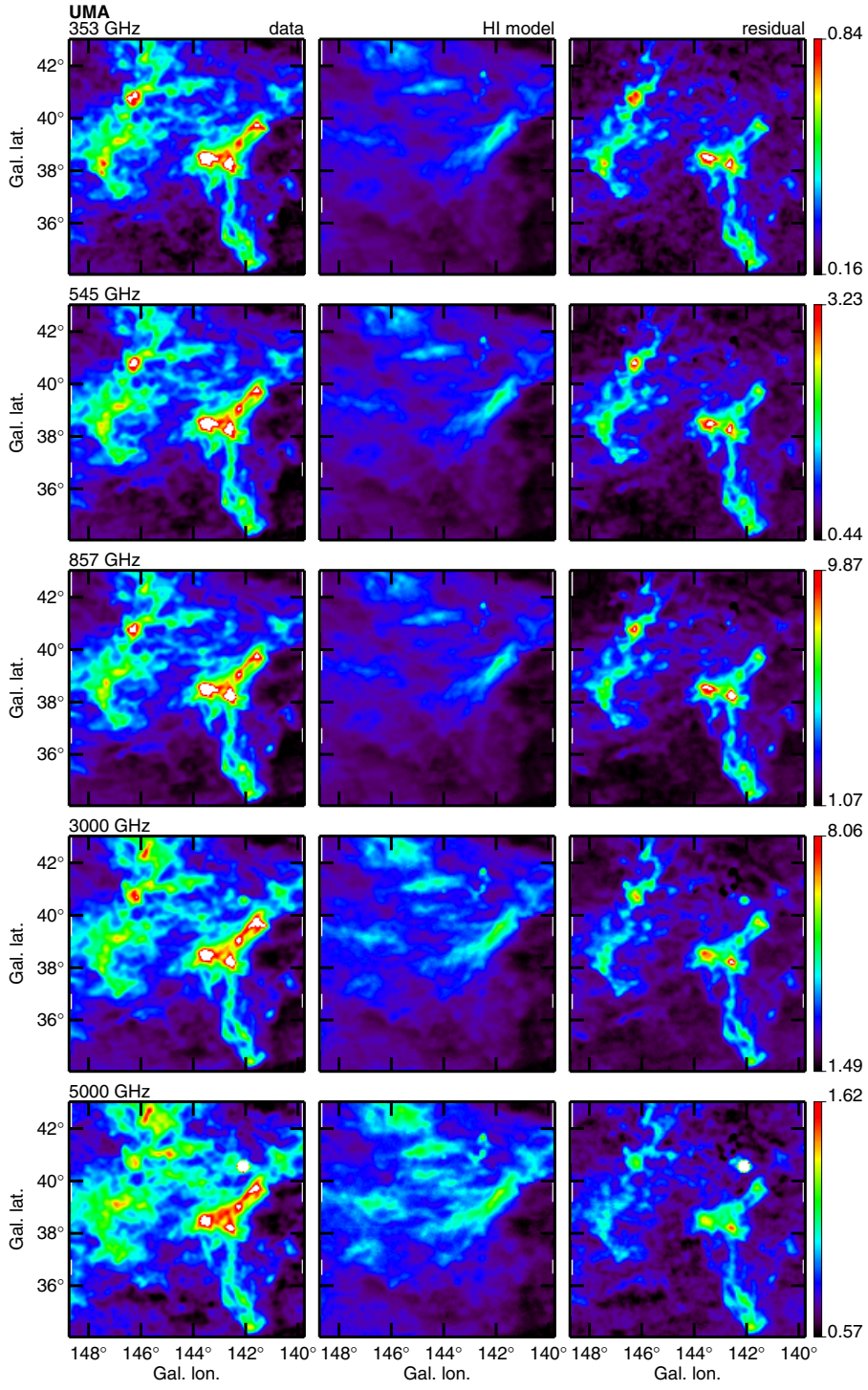

Fig. 8. Like Fig. 4, for field UMA.

and temperature but for typical interstellar conditions for CNM gas ($n = 100\,\mathrm{cm}^{-3}$, $T = 80\,\mathrm{K}$, $G = 1$, where G is the scaling factor of the InterStellar Radiation Field (ISRF) as defined by Mathis et al. (1983)), it is about $N_{\mathrm{HI}} = 2.5 \times 10^{20}\,\mathrm{cm}^{-2}$ (Reach et al. 1998). Others have used a quadratic function for ϵ_ν (Fixsen et al. 1998) based on the idea that the H_2 column density depends (at least dimensionally) on N_{HI}^2 (Reach et al. 1994). Both methods introduce a bias in the parameter estimation that is difficult to quantify.

Instead of applying an arbitrary cutoff in N_{HI}, Arendt et al. (1998) used an iterative method to exclude data points above a cut along lines perpendicular to the fit, in order to arrive at a stable solution for ϵ_ν. We used a similar approach by iteratively masking out data points that would produce a positively-skewed residual. That way we expect to keep pixels in the maps that correspond to lines of sight where the dust emission is dominated by the atomic H I components.

The PDF of residual map, R, defined as

$$R_\nu(x,y) \equiv I_\nu(x,y) - \sum_{i=1}^{3} \epsilon_\nu^i N_{\mathrm{HI}}^i(x,y) - Z_\nu, \quad (6)$$

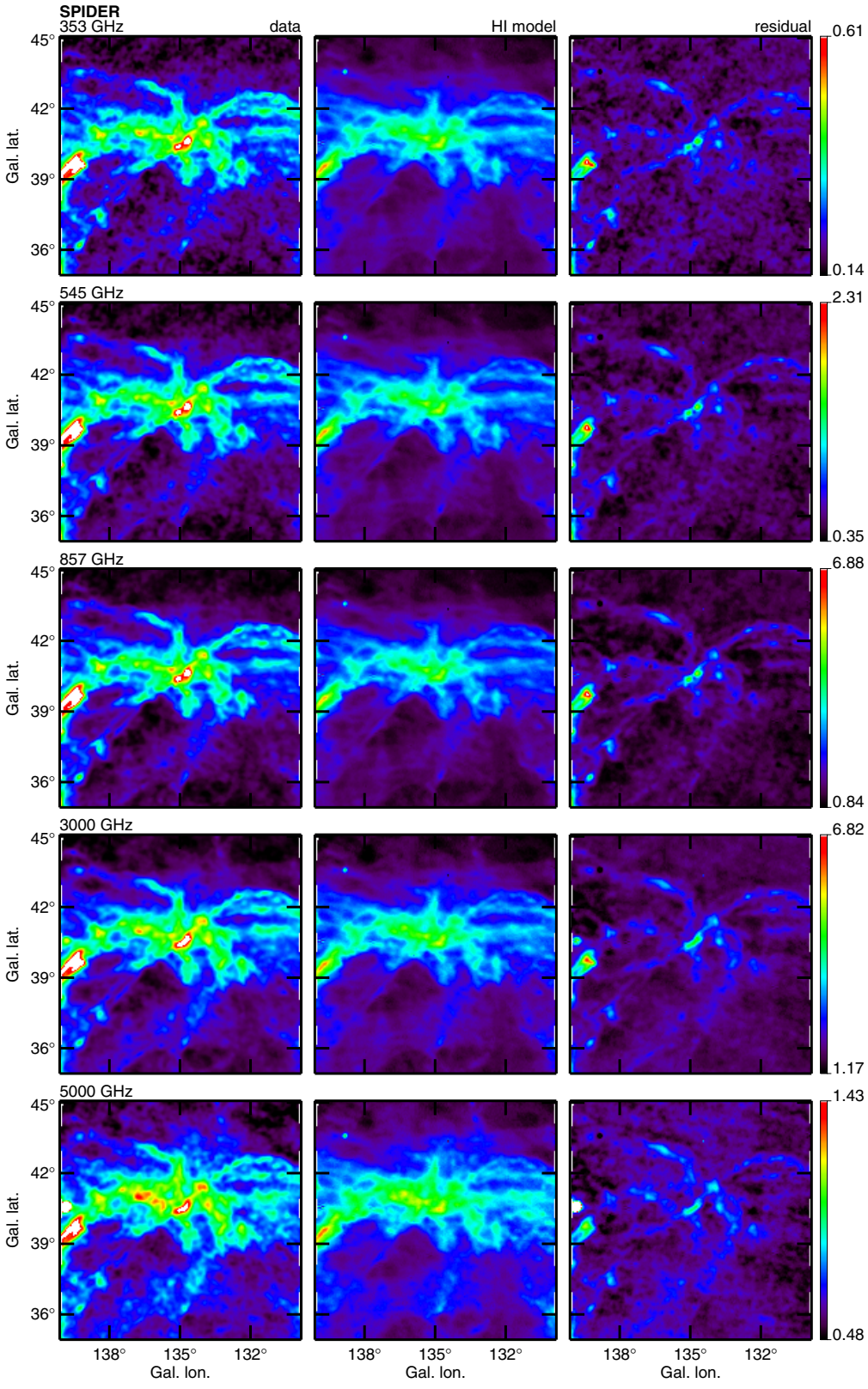

Fig. 9. Like Fig. 4, for field SPIDER.

is used to estimate the mask. We used the *Planck* 857-GHz channel because it has the best signal-to-noise ratio and is less sensitive than the IRAS channels to dust temperature-induced emissivity variations. For the most diffuse fields in our sample (AG, MC, N1, BOOTES, G86, SP) the PDF of R_{857} is very close to a Gaussian, which suggests that the model described by Eq. (2) is the right one in such low column density regions.

Accordingly, for the first iteration of the masking process for each field, we performed the multi-variate linear regression based on Eqs. (3) to (5) using only the faintest 10% pixels in the

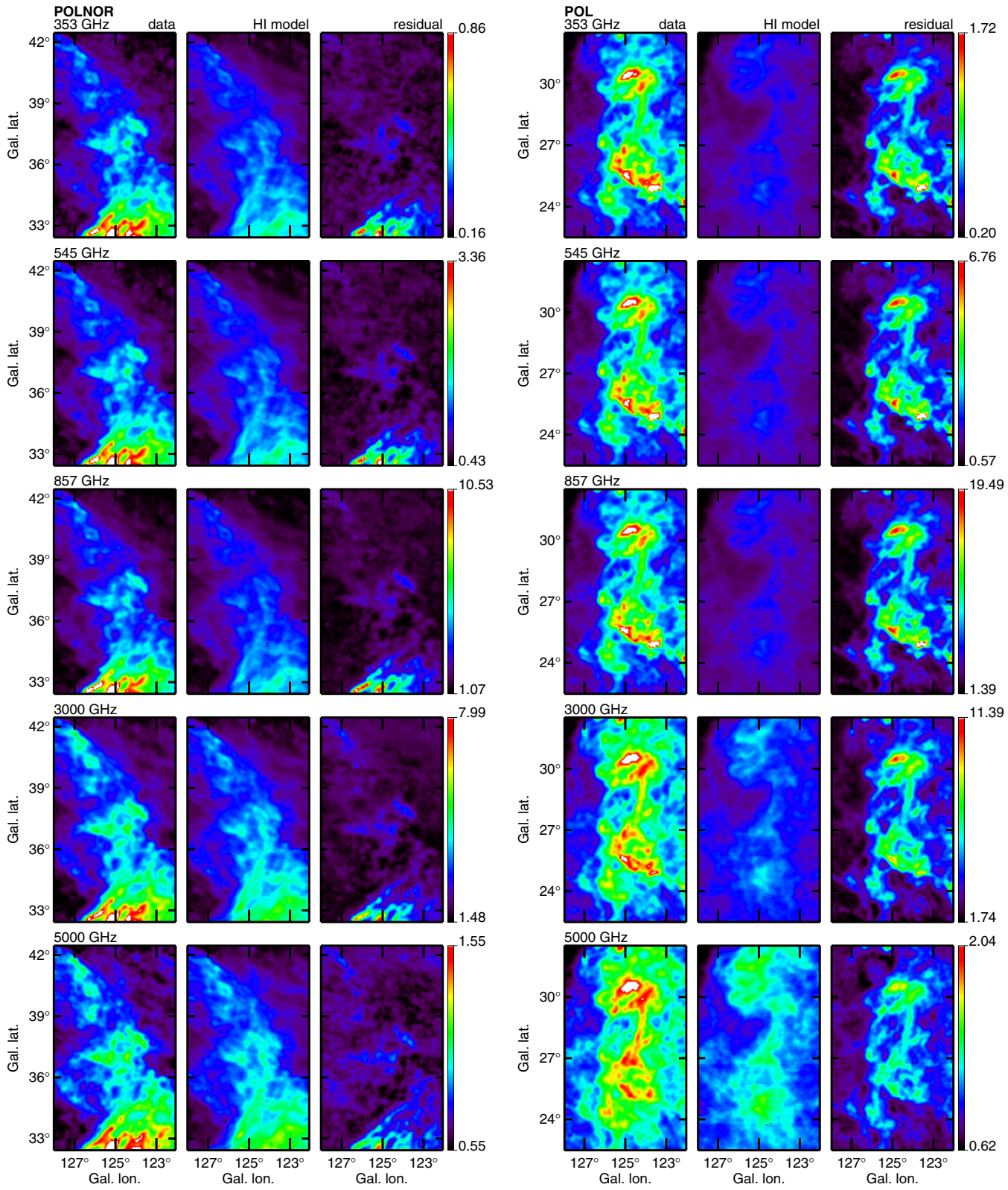

Fig. 10. Like Fig. 4, for fields POLNOR (*left*) and POL (*right*).

857 GHz map. For further iterations this threshold was relaxed, bringing in more pixels in the map compatible with the iterated model.

As discussed above, the presence of dust emission associated with molecular gas can positively skew the PDF, and empirically the PDF of R_{857} is indeed positively skewed for the eight remaining fields (Fig. 12). To determine the set of pixels to be retained, we used a Gaussian fit to the lower, rising part of the PDF, up to the PDF maximum, and estimated the σ (see the red curves in Fig. 12). With the above motivation, we assume that the lower part of the PDF is representative of pixels where the fit works well (i.e., for these pixels the residual is normally distributed).

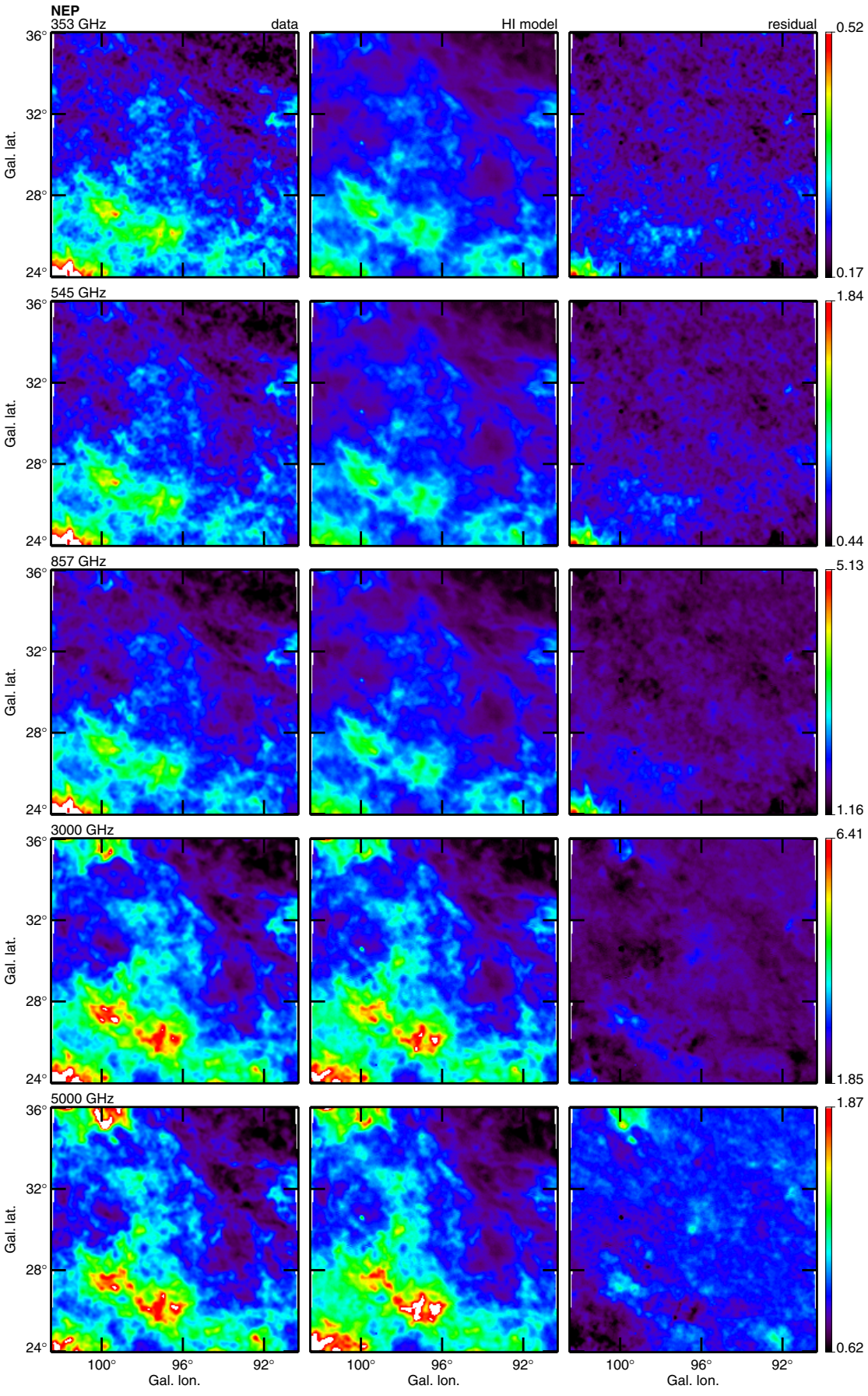

Fig. 11. Like Fig. 4, for field NEP, the largest.

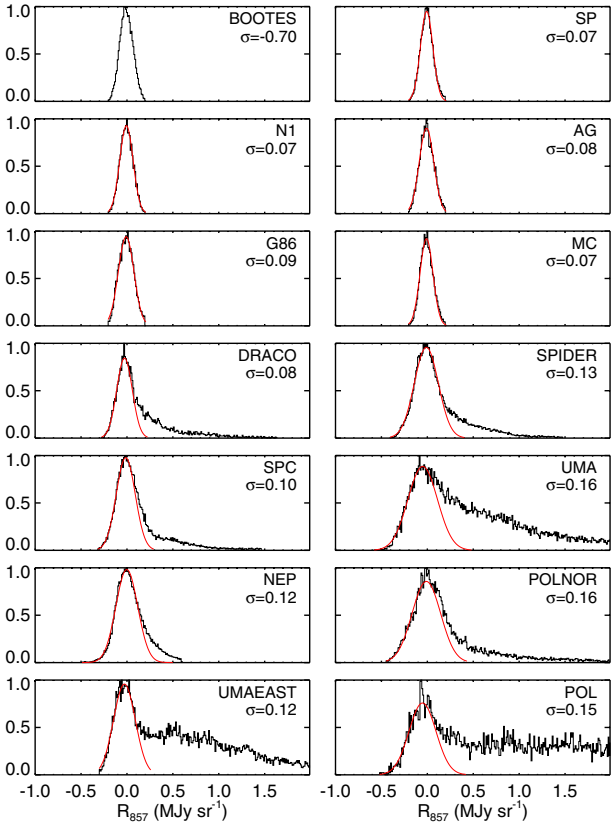

Fig. 12. Normalised PDF of the residual R_{857} of the dust-gas correlation at 857 GHz for each field after convergence of the masking procedure. The red curve is the result of a Gaussian fit to the lower, rising part of the PDF.

Using the σ fit only to this part of the PDF, we apply a threshold in R_{857} by masking out all pixels with $R_{857} > 3 \times \sigma$ away from the mean. We iteratively recompute the parameters and mask to converge on a stable solution. The PDFs of R_{857} obtained at the end of the process are shown in Fig. 12.

For the six faintest fields, the masking excluded less than 1% of the points. For these fields the mask has no significant effect on the estimated parameters. For the eight other fields, the masking method excluded from 17 to 83% of the pixels. The masks for these eight fields are shown in Fig. 13. In these cases the masking has a significant effect on the result, but we have checked that the estimated parameters are similar to the ones obtained with a $N_{\rm HI} \leq 4 \times 10^{20}\,{\rm cm}^{-2}$ threshold. In fact the masking method used here allows us to keep pixels that would have been excluded by a simple $N_{\rm HI}$ thresholding even though they do not depart significantly from the linear correlation.

Table 2 provides the ϵ_ν^i values for each field/component/frequency. In order to visualize the results, Fig. 14 gives scatter plots together with the line of slope ϵ_{857}^i for each component, field by field. Specifically, for each HI component i we plotted $I_\nu - \sum_{j\neq i} \epsilon_j N_{\rm HI}^j - Z_\nu$ as a function of $N_{\rm HI}^i$.

4.4. Statistics of the residual

Figures 4 to 11 show the IRAS and *Planck* maps, together with the H I correlated emission and the residual maps R_ν for all our fields. For the six faintest fields (N1, SP, BOOTES, AG, MC, and G86 – see Figs. 4–5), the structure in the residuals is, even by visual inspection, clearly spatially correlated between frequencies, especially in the *Planck* bands. It is dominated by small scale structures with equally negative and positive brightness fluctuations. The structure of the residual for brighter fields is also clearly correlated between frequencies but in these cases the residual is mostly positive (i.e., they are excesses with respect to the H I). These residuals also show larger coherent structures than in the fainter fields.

The rms (about the mean) of the residual R can be approximated as:

$$\sigma_R = \sqrt{\sigma_S^2 + (\sigma_{\rm noise}^{\rm dust})^2 + \sum_{i=1}^{3} (\epsilon_\nu^i \delta N_{\rm HI}^i)^2}, \quad (7)$$

where noise in the IRAS or *Planck* data and that induced by uncertainties in $N_{\rm HI}$ are explicitly accounted for and σ_S includes all other contributions not in the model, including CIB anisotropies and dust emission associated with molecular gas. After quadratic subtraction Fig. 15 shows the value of σ_S at each frequency, as a function of the average $N_{\rm HI}$ density for each field. For fields with a median column density lower than $2 \times 10^{20}\,{\rm cm}^{-2}$, the PDFs of the residual emission all have skewness and kurtosis values compatible with a Gaussian distribution. Furthermore the width of these PDFs shows very small scatter from field to field (see Fig. 15). This is another indication that, for such diffuse fields, the model is a good description of the data; i.e., the Galactic dust emission is largely dominated by the H I components, with very limited spatial variations of the emissivity across a given field.

The dashed line gives the average level of σ_S for those fields with $N_{\rm HI} < 2 \times 10^{20}\,{\rm cm}^{-2}$. These quantities, together with the average *Planck* or IRAS and GBT noise contributions to σ_R, are summarized in Table 3. It is clear from Table 3 and Fig. 15 that even for faint fields σ_S is the main contributor to the rms of the residual, and therefore the main contributor to the dispersion in the dust-gas correlation diagrams in these fields. This is in accordance with the findings of Planck Collaboration (2011n) who concluded that the CIB fluctuations dominate σ_S at 353 GHz and higher frequencies.

At higher column densities, the PDF of the residual shows positive skewness and an rms that increases with $N_{\rm HI}$, significantly exceeding the level of CIB anisotropies. These aspects of the PDF indicate one or more extra components that contribute to the dust emission and are not taken into account in our model. Contributions to the residual that grow with $N_{\rm HI}$ are compatible with the presence of a molecular gas component. This could also come from spatial variations of the dust emissivity for given H I components or from inadequately-separated H I components.

4.5. Monte-Carlo method to determine emissivity uncertainties

The statistical uncertainties estimated for the emissivities by the least-squares fit method are accurate only for the case of white Gaussian noise in I_ν and (sufficiently) low noise in the $N_{\rm HI}$ components. The noise in I_ν includes IRAS or *Planck* instrumental noise, CIB anisotropies, and various interstellar contaminants, and for the most diffuse fields in our sample, its PDF is close to Gaussian. However, its power spectrum is certainly not white. First, at the angular scales of our observations (from 9′ to a few degrees), the power spectrum of the CIB anisotropies is $P(k) \propto k^{-1}$ (Planck Collaboration 2011n). Second, the spatial variation of the coverage and the convolution to the GBT resolution both introduce spatial structure in the noise that modifies

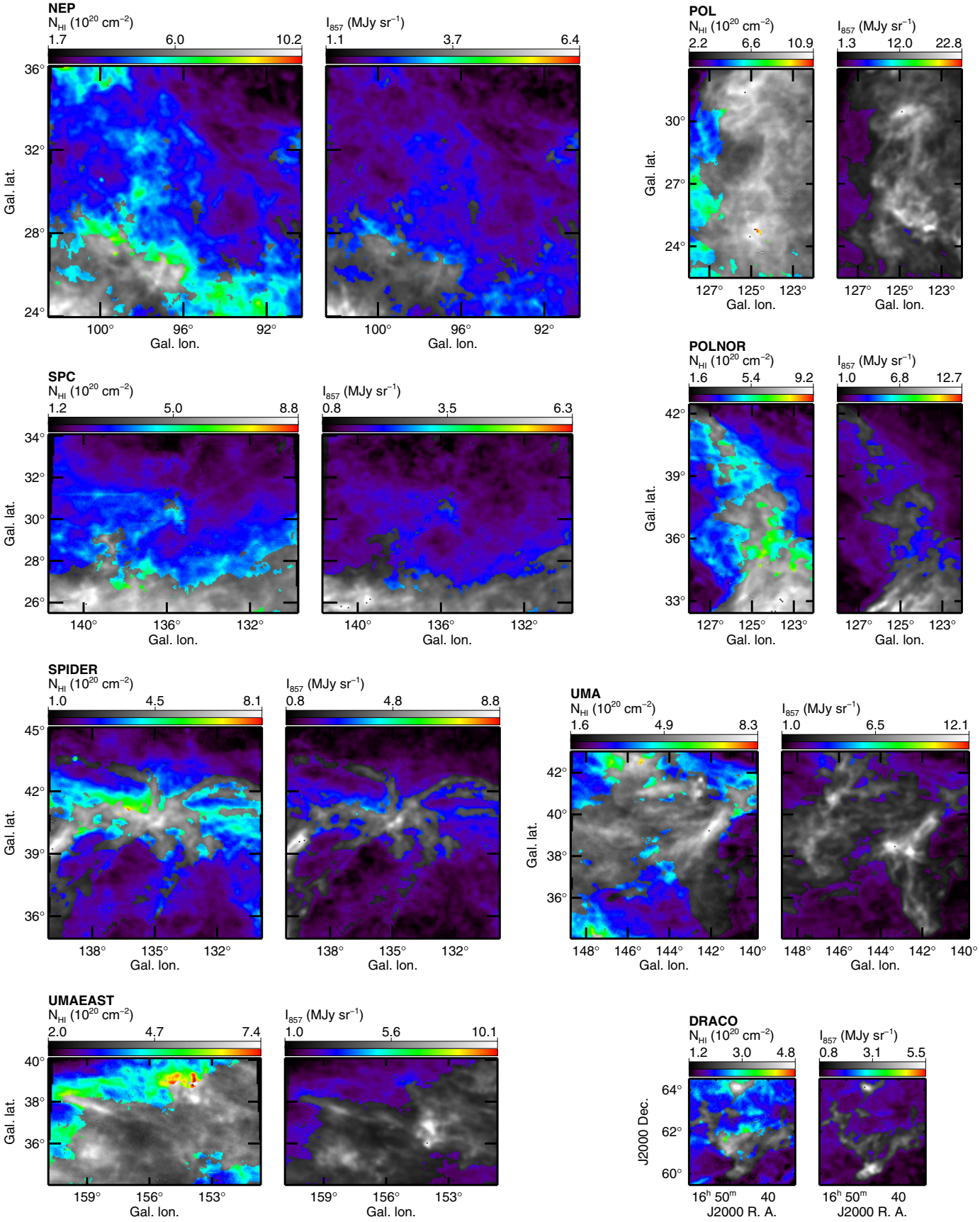

Fig. 13. Mask for the eight fields where more than 1% of the pixels were excluded (NEP = 17%, POL = 83%, SPC = 26%, POLNOR = 30%, SPIDER = 24%, UMA = 56%, UMAEAST = 66%, DRACO = 29%). For each field the *left* image is the total H I integrated emission and the *right* image is the *Planck* 857 GHz map. The regions in greyscale were excluded from the correlation analysis. Note the relationship of the masks to the regions of high residual in Figs. 5 to 11.

Table 2. Emissivities of each H I component at 353, 545, 857, 3000, and 5000 GHz.

Field	HI	ϵ_{353}	ϵ_{545}	ϵ_{857}	ϵ_{3000}	ϵ_{5000}
AG	LVC	0.034 ± 0.007	0.14 ± 0.02	0.39 ± 0.05	0.68 ± 0.04	0.181 ± 0.018
	IVC	0.020 ± 0.005	0.075 ± 0.016	0.22 ± 0.03	0.58 ± 0.03	0.161 ± 0.013
	HVC	0.004 ± 0.003	0.011 ± 0.008	0.018 ± 0.015	0.037 ± 0.015	0.009 ± 0.006
BOOTES	LVC	0.045 ± 0.010	0.17 ± 0.03	0.54 ± 0.06	0.95 ± 0.08	0.23 ± 0.03
	IVC	0.029 ± 0.007	0.12 ± 0.02	0.37 ± 0.04	0.87 ± 0.05	0.275 ± 0.020
	HVC	0.02 ± 0.02	0.09 ± 0.07	0.20 ± 0.13	−0.30 ± 0.18	−0.13 ± 0.07
DRACO	LVC	0.043 ± 0.011	0.18 ± 0.04	0.49 ± 0.07	0.57 ± 0.07	0.08 ± 0.02
	IVC	0.042 ± 0.004	0.168 ± 0.013	0.48 ± 0.03	0.70 ± 0.03	0.167 ± 0.009
	HVC	0.007 ± 0.006	0.032 ± 0.018	0.07 ± 0.04	0.10 ± 0.04	0.025 ± 0.013
G86	LVC	0.033 ± 0.004	0.146 ± 0.012	0.45 ± 0.02	0.71 ± 0.03	0.165 ± 0.008
	IVC	0.0151 ± 0.0019	0.070 ± 0.006	0.238 ± 0.013	0.643 ± 0.015	0.206 ± 0.004
	HVC	−0.05 ± 0.02	−0.19 ± 0.07	−0.36 ± 0.16	−0.24 ± 0.19	−0.09 ± 0.05
MC	LVC	0.031 ± 0.010	0.15 ± 0.03	0.45 ± 0.06	0.78 ± 0.07	0.18 ± 0.03
	IVC	0.008 ± 0.009	0.02 ± 0.03	0.16 ± 0.05	0.70 ± 0.06	0.17 ± 0.03
	HVC	−0.006 ± 0.002	−0.020 ± 0.007	−0.047 ± 0.015	−0.030 ± 0.017	0.019 ± 0.007
N1	LVC	0.056 ± 0.007	0.215 ± 0.020	0.58 ± 0.04	0.86 ± 0.03	0.166 ± 0.011
	IVC	0.039 ± 0.007	0.15 ± 0.02	0.41 ± 0.04	0.72 ± 0.03	0.213 ± 0.012
	HVC	0.005 ± 0.004	0.015 ± 0.014	0.04 ± 0.03	−0.01 ± 0.02	−0.001 ± 0.007
NEP	LVC	0.0420 ± 0.0014	0.163 ± 0.005	0.470 ± 0.011	0.664 ± 0.013	0.141 ± 0.005
	IVC	0.0197 ± 0.0012	0.080 ± 0.004	0.236 ± 0.010	0.666 ± 0.013	0.229 ± 0.004
	HVC	−0.021 ± 0.009	−0.09 ± 0.03	−0.22 ± 0.07	−0.43 ± 0.10	−0.02 ± 0.03
POL	LVC	0.0519 ± 0.0019	0.203 ± 0.007	0.57 ± 0.02	0.455 ± 0.018	0.102 ± 0.004
	IVC	0.056 ± 0.012	0.24 ± 0.05	0.61 ± 0.13	0.72 ± 0.11	0.18 ± 0.03
	HVC	–	–	–	–	–
POLNOR	LVC	0.0476 ± 0.0012	0.200 ± 0.004	0.612 ± 0.012	0.538 ± 0.012	0.088 ± 0.003
	IVC	0.023 ± 0.007	0.08 ± 0.02	0.20 ± 0.07	0.51 ± 0.07	0.156 ± 0.016
	HVC	–	–	–	–	–
SP	LVC	0.063 ± 0.008	0.25 ± 0.03	0.72 ± 0.05	0.59 ± 0.04	0.094 ± 0.016
	IVC	0.029 ± 0.008	0.11 ± 0.02	0.29 ± 0.05	0.77 ± 0.04	0.229 ± 0.016
	HVC	−0.003 ± 0.007	−0.02 ± 0.02	−0.07 ± 0.04	−0.12 ± 0.04	−0.042 ± 0.013
SPC	LVC	0.0365 ± 0.0017	0.140 ± 0.005	0.401 ± 0.011	0.411 ± 0.011	0.086 ± 0.004
	IVC	0.015 ± 0.008	0.06 ± 0.02	0.18 ± 0.05	0.54 ± 0.05	0.197 ± 0.020
	HVC	−0.004 ± 0.005	−0.005 ± 0.017	0.00 ± 0.04	−0.05 ± 0.04	−0.005 ± 0.013
SPIDER	LVC	0.0474 ± 0.0014	0.200 ± 0.004	0.602 ± 0.012	0.570 ± 0.013	0.093 ± 0.004
	IVC	0.030 ± 0.003	0.107 ± 0.012	0.30 ± 0.03	0.59 ± 0.03	0.162 ± 0.009
	HVC	−0.056 ± 0.016	−0.17 ± 0.05	−0.52 ± 0.14	−0.80 ± 0.16	−0.10 ± 0.04
UMA	LVC	0.049 ± 0.002	0.211 ± 0.007	0.62 ± 0.02	0.563 ± 0.017	0.098 ± 0.005
	IVC	0.030 ± 0.005	0.12 ± 0.02	0.37 ± 0.06	0.58 ± 0.05	0.151 ± 0.012
	HVC	−0.013 ± 0.005	−0.064 ± 0.019	−0.18 ± 0.05	−0.12 ± 0.04	−0.006 ± 0.011
UMAEAST	LVC	0.031 ± 0.003	0.147 ± 0.008	0.48 ± 0.02	0.566 ± 0.016	0.106 ± 0.005
	IVC	0.059 ± 0.004	0.219 ± 0.014	0.59 ± 0.04	0.65 ± 0.03	0.191 ± 0.009
	HVC	0.007 ± 0.004	0.024 ± 0.013	0.06 ± 0.03	0.04 ± 0.03	0.008 ± 0.008

Notes. Units are MJy sr^{-1}/10^{20} cm^{-2}. The uncertainties were obtained using Monte-Carlo simulations (see Sect. 4.5).

Table 3. Average of the standard deviations of the sky residual σ_S for the six fields with $\langle N_{HI}\rangle$ lower than 2×10^{20} cm^{-2} (AG, BOOTES, G86, MC, N1, and SP).

ν (GHz)	σ_S (MJy sr^{-1})	σ^{dust}_{noise} (MJy sr^{-1})	σ^{HI}_{noise} (MJy sr^{-1})
353	0.0120 ± 0.0006	0.0060 ± 0.0012	0.0014 ± 0.0006
545	0.038 ± 0.002	0.0096 ± 0.0018	0.006 ± 0.003
857	0.074 ± 0.006	0.0097 ± 0.0019	0.016 ± 0.007
3000	0.077 ± 0.017	0.028 ± 0.004	0.022 ± 0.005
5000	0.027 ± 0.006	0.0146 ± 0.0016	0.0053 ± 0.0010

Notes. σ^{dust}_{noise} is the average level of noise rms in the IRAS and *Planck* maps at the GBT resolution (i.e., noise level in maps convolved at 9.4′) computed for the 14 fields. σ^{HI}_{noise} gives the average GBT noise converted to MJy sr^{-1} (see Eq. (7)), for the 14 fields. All uncertainties are the 1σ value of each sample.

its power spectrum. The addition of all those noise sources produces a net noise term n_ν on I_ν that is not white. Because of the random chance correlation of n_ν with the N_{HI} components, the uncertainties on the parameters estimated from the least-squares are systematically underestimated (the least-squares fit is not optimal). In addition, the N_{HI} maps are not noise free; significant noise on the independent variable in a least-squares fit produces a systematic bias in the solution. Furthermore, imperfect opacity correction of the H I spectra, the presence of molecular gas, and spatial variations of the dust properties will also produce non-random fluctuations in the residual map. For all of these reasons, an analysis of Monte-Carlo simulations is required for proper estimation of the uncertainties and biases in the ϵ^i_ν.

To generate simulations for each field, we adopted the N_{HI} maps obtained from the 21-cm observations as templates of the dust emission. We built dust maps I'_ν for each frequency ν by adding up these N_{HI} maps multiplied by their respective estimated emissivities ϵ^i_ν (just as in computing the residual), to which we added realizations of the IRAS or *Planck* noise n_ν appropriate to the field[4] at a level compatible with Table 3 once

[4] We assumed white noise maps for both IRAS and *Planck*, each divided by the square root of their coverage map.

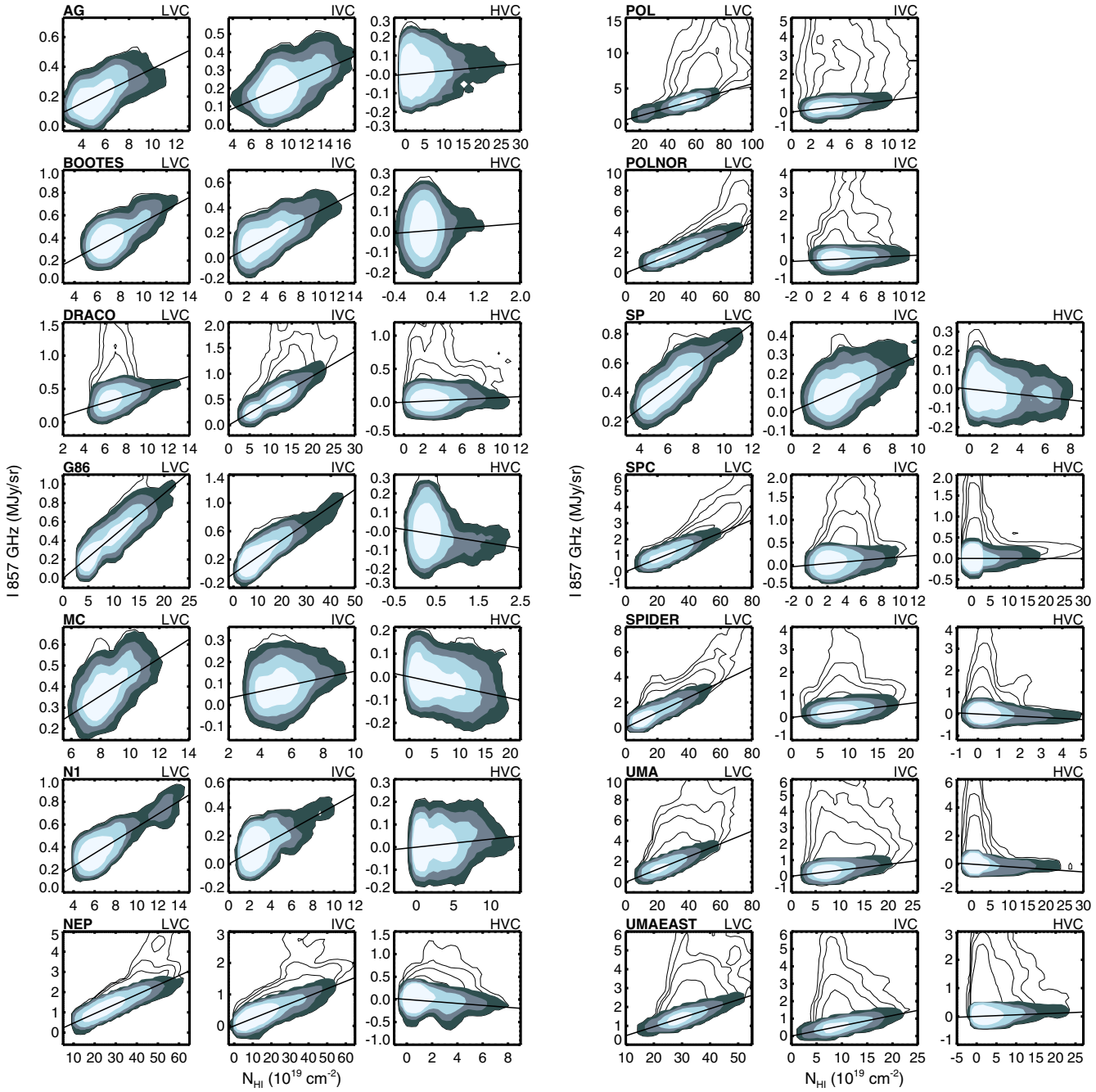

Fig. 14. I_{857} vs. $N_{\rm HI}$ scatter plots, visualising the dust-gas correlation for each of the three H I components, across a row. The fields POL and POLNOR do not have an HVC component. For a given H I component, the remaining 857 GHz emission, once the contribution of the other two H I components has been removed, is plotted as a function of $N_{\rm HI}$ of that component (i.e., $I_\nu - \sum_{j\neq i} \epsilon_j N^j_{\rm HI} - Z_\nu$ as a function of $N^i_{\rm HI}$). The contours show quartiles of the density of points in each scatter plot. The filled contours show the data points used in the correlation analysis (i.e., data points not masked out) while the open contours show all data points.

convolved at GBT resolution, and of the sky residual a_ν with a k^{-1} power spectrum at a level to reproduce σ_S within the mask[5]:

$$I'_\nu = \sum_{i=1}^{3} \epsilon^i_\nu N^i_{\rm HI} + a_\nu + n_\nu. \quad (8)$$

[5] For the faintest fields this will produce a map with the statistical properties of the CIB anisotropies. For brighter fields, where the residual also includes interstellar contributions, we assumed it also follows a k^{-1} power spectrum, but with a greater normalisation (i.e., σ_S) to take into account these effects.

Before fitting these simulated data we added white noise to each $N_{\rm HI}$ component at the level estimated for the GBT data (Table 1). We then carried out the least-squares fit, using the mask already estimated for each field. From a thousand such simulations for each field, we obtained the statistics of the recovered $\epsilon^{i\prime}_\nu$ so that we could determine if our original fit (fed into the simulation) was biased and could compare the dispersion of the parameters to the statistical uncertainties returned by the least-squares fitting procedure.

Table 4 summarizes the results of the Monte-Carlo simulations. Due to random correlation between n_ν and the $N_{\rm HI}$

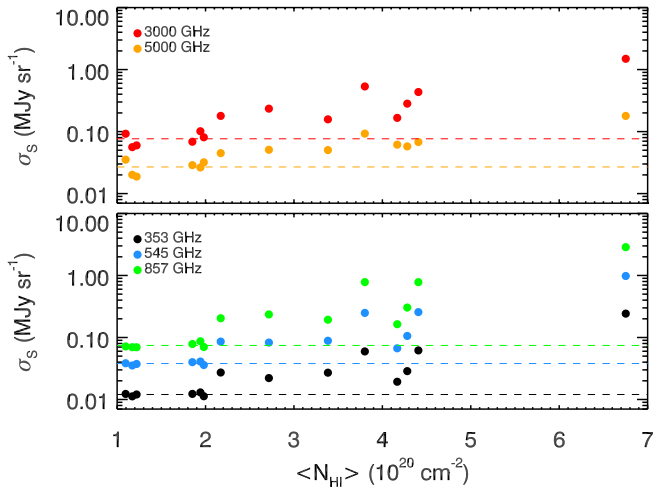

Fig. 15. Value of σ_S obtained from the standard deviation σ_R of the residual maps $R_\nu(x, y)$ from which contributions from the IRAS or *Planck* and the GBT noise were removed quadratically (see Eq. (7)), plotted as a function of the average HI column density of each field (sum of LVC, IVC and HVC). The dashed line is the average of σ_S for fields with $N_{\rm HI} < 2 \times 10^{20}$ cm^{-2} (see Table 3).

components, we find the Monte-Carlo-derived uncertainty in ϵ_ν^i is several times higher than the analytically-derived uncertainty. The results are reported in the table in terms of ϕ_ν, the ratio of $\sigma(\epsilon_\nu^{i\prime})$, the standard deviation of the emissivities recovered in the simulations, to $\delta\epsilon_\nu^i$, the standard deviation expected from the linear fit performed by *Regress*. Therefore, in what follows we use the values of $\sigma(\epsilon_\nu^{i\prime})$ as the uncertainties in ϵ_ν^i (see Table 2).

Finally, these simulations make it possible for us to estimate any bias in ϵ_ν^i which could arise from the noise in $N_{\rm HI}$. Table 4 also provides the bias in %: $b_\nu = 100(\langle\epsilon_\nu^\prime\rangle - \epsilon_\nu)/\epsilon_\nu$. Except for some (undetected) HVCs, the bias is only at the few percent level; in what follows we made no correction for it.

5. Results

5.1. Planck and IRAS emissivities

The present study extends to smaller scales, and to the IVCs and HVCs, the earlier work done with the FIRAS (Boulanger et al. 1996) or IRAS (Boulanger & Pérault 1988; Reach et al. 1998) data on the dust emission of the diffuse ISM. It also extends to a much larger sample a similar analysis done on a diffuse $3^\circ \times 3^\circ$ region at high Galactic latitude using IRAS and *Spitzer* data (Miville-Deschênes et al. 2005). The IR/submm-H I correlation analysis allows us to determine empirically the spectral dependence of the ratio between the dust emission and the gas column density. In addition, the combination of *Planck*, IRAS, and $N_{\rm HI}$ data can be used to trace one elusive component of the diffuse interstellar medium: the diffuse H_2 gas (Sect. 6.1).

As seen in Fig. 14 there is a clear correlation between the IRAS or *Planck* data and $N_{\rm HI}$ in all fields but, as previously seen with COBE and IRAS data, there are increasing excesses of dust emission with increasing $N_{\rm HI}$. The estimated emissivities for each field/component/frequency are compiled in Table 2 and shown in Fig. 16. We note that dust associated with the LVC and IVC components is detected in each field and at each frequency, unlike for HVCs for which we do not report any significant detection. All HVC emissivities are indeed below 3σ. The results on HVCs are discussed further in Sect. 6.3. In the following we analyse what can be drawn from the emissivities for the LVCs and IVCs.

5.2. Comparison with FIRAS data

The FIRAS data provide a reference for the dust emission spectrum of the diffuse ISM. The average FIRAS SED of the high-Galactic latitude sky used by Compiègne et al. (2011) to set the diffuse ISM dust properties in the DustEM model is shown in Fig. 17. Also shown in this figure are the current results (red symbols) for the average of the emissivities for the LVCs of our sample at 353, 545, 857, 3000, and 5000 GHz. The IRAS and *Planck* data points are found to be fully compatible with the diffuse ISM FIRAS spectrum, showing that our sample is representative of the diffuse dust emission at high Galactic latitudes. We have fit model parameters to both data sets independently using a modified black body function:

$$\epsilon_\nu = I_\nu / N_{\rm HI} = \kappa_0 (\nu/\nu_0)^\beta \mu m_{\rm H} B_\nu(T), \quad (9)$$

where $B_\nu(T)$ is the Planck function, $m_{\rm H}$ the mass of hydrogen, μ the mean molecular weight and κ_0 is the opacity of the dust–gas mixture at some fiducial frequency ν_0. The higher-frequency (60 μm) IRAS datum is not used in the fit due to contamination by non-equilibrium emission from stochastically-heated smaller grains (Compiègne et al. 2011). The top panel of Fig. 17 shows the data divided by the model to better display the quality of the fit. The values found for T and β with the two data sets are in close accord. This analysis shows that the local ISM SED can be fit well with $T = 17.9$ K and $\beta = 1.8$.

5.3. The spectral energy distribution

Figure 16 shows the dust SED for each field and H I component separately, with the error bars computed using the Monte-Carlo simulations. We first note that all the LVC and IVC SEDs are at a similar level showing that the power emitted per H is comparable between fields. Second, in many cases, the SED of IVCs peaks at a higher frequency than for the LVCs. That could be caused by a higher temperature or a larger abundance of smaller grains in the IVCs.

Like for the FIRAS comparison, each SED was fit using a modified black body function (solid lines). It has been shown by several studies (Dupac et al. 2003; Désert et al. 2008; Shetty et al. 2009; Veneziani et al. 2010) how difficult it is to estimate separately T and β for such an SED fit. These two parameters are significantly degenerate; their estimate depends greatly on the accuracy of the determination of the error bars on the SED data points and on the correlation of the errors between frequencies. The estimate of T and β also depends on the spectral range used to make the fit; for a typical $T = 18$ K dust emission spectrum, the Rayleigh-Jeans range of the black body curve, where β can be well estimated, corresponds to $\nu < 375$ GHz ($\lambda > 800\,\mu$m).

Because of the above caveats relating to simultaneous fits of T and β, and because the FIRAS spectrum of the diffuse ISM is compatible with $\beta = 1.8$ (in this case the large number of data points and the broad frequency coverage over the peak of the SED give more confidence in the value of β obtained), we have carried out SED fitting assuming a fixed $\beta = 1.8$. This provides a direct way to compare not only with the FIRAS spectrum and the DustEM model, but also with similar analyses with *Planck* data on molecular clouds and in the Galactic plane (Planck Collaboration 2011o,q,u) that used the same convention.

Table 4. Results from the Monte-Carlo simulations.

Field	HI	δ_{353}	δ_{545}	δ_{857}	δ_{3000}	δ_{5000}	ϕ_{353}	ϕ_{545}	ϕ_{857}	ϕ_{3000}	ϕ_{5000}	b_{353}	b_{545}	b_{857}	b_{3000}	b_{5000}
AG	LVC	0.98	0.98	0.99	0.98	1.03	6.35	6.75	6.57	5.91	6.41	−3.05	−3.99	−4.12	−4.49	−4.46
	IVC	0.99	0.99	1.01	0.99	1.04	7.02	6.88	7.69	6.61	7.06	1.67	2.12	1.75	0.74	0.37
	HVC	1.00	1.00	1.02	1.00	1.05	7.66	7.78	7.98	7.60	7.78	−0.05	5.81	7.94	7.16	3.47
BOOTES	LVC	0.99	0.99	1.01	0.96	0.93	10.39	11.63	12.41	11.27	10.87	−1.50	−1.72	−1.65	−1.69	−1.40
	IVC	1.00	1.00	1.01	0.97	0.93	12.37	13.14	13.64	13.24	11.86	−0.41	−0.05	−0.56	−0.79	−1.19
	HVC	0.86	0.86	0.87	0.83	0.80	4.21	4.56	4.75	4.47	4.08	−22.91	−18.63	−20.17	−30.00	−29.46
DRACO	LVC	1.00	0.98	1.06	1.01	1.02	7.14	7.33	7.64	7.22	7.45	−0.24	−1.26	−0.44	−1.89	−2.74
	IVC	1.00	0.99	1.06	1.02	1.03	8.16	7.90	8.91	8.13	7.97	−0.14	−0.47	−0.23	−0.53	−0.47
	HVC	0.99	0.97	1.05	1.00	1.01	5.59	5.41	6.01	5.59	5.53	−0.34	−2.68	−3.08	−5.46	−5.56
G86	LVC	0.99	0.99	1.02	0.98	1.01	8.46	8.80	8.85	8.92	8.22	0.97	0.35	0.44	0.04	0.36
	IVC	1.01	1.01	1.03	1.00	1.02	7.86	8.24	8.39	8.27	7.84	0.18	0.12	−0.24	−0.05	−0.01
	HVC	0.93	0.93	0.95	0.92	0.94	5.57	5.65	5.96	5.61	5.53	−14.85	−15.52	−15.52	−16.60	−11.00
MC	LVC	0.98	0.99	1.00	0.99	0.98	7.61	8.91	9.46	8.88	8.54	−3.36	−4.07	−3.31	−3.51	−1.98
	IVC	0.99	1.00	1.00	1.00	0.98	6.18	6.88	7.35	6.96	6.73	0.19	−2.80	−1.74	−2.17	−1.97
	HVC	0.99	1.00	1.01	1.00	0.99	6.62	7.42	8.17	7.57	7.60	−4.35	−2.57	−1.38	−3.01	−0.14
N1	LVC	0.99	0.99	0.99	1.00	1.02	7.22	7.50	7.52	7.04	6.77	−2.10	−1.98	−2.25	−1.90	−2.02
	IVC	0.99	1.00	1.00	1.00	1.03	7.62	7.99	8.07	7.28	7.46	−1.56	−0.95	−1.67	−1.47	−1.54
	HVC	0.99	1.00	1.00	1.00	1.03	7.87	8.24	8.25	7.91	7.51	−5.16	−2.03	−8.00	6.82	10.14
NEP	LVC	0.99	0.98	0.99	0.91	0.75	10.11	10.21	10.23	9.14	7.51	−0.25	−0.20	−0.23	−0.30	−0.15
	IVC	0.99	0.99	1.00	0.92	0.76	11.86	12.00	12.52	11.46	9.10	−0.07	−0.25	−0.10	−0.09	−0.03
	HVC	0.97	0.97	0.98	0.90	0.74	9.83	10.33	9.76	9.39	7.63	−6.53	−4.58	−3.86	−3.82	−11.00
POL	LVC	0.98	0.98	0.99	0.98	0.99	6.62	7.09	7.03	7.15	6.78	−0.02	−0.20	−0.23	−0.04	0.20
	IVC	0.96	0.97	0.98	0.96	0.98	6.06	6.43	6.52	6.46	6.32	−2.20	−3.05	−1.61	−3.05	−3.38
	HVC	–	–	–	–	–	–	–	–	–	–	–	–	–	–	–
POLNOR	LVC	1.01	1.01	1.02	1.01	1.03	8.97	9.28	9.61	9.11	8.96	−0.17	−0.08	−0.13	−0.21	−0.14
	IVC	1.00	1.01	1.01	1.00	1.02	8.14	8.04	7.96	8.34	7.75	−3.14	−1.36	−2.17	−1.66	−1.69
	HVC	–	–	–	–	–	–	–	–	–	–	–	–	–	–	–
SP	LVC	0.98	0.99	1.00	0.99	1.03	8.17	8.63	8.82	7.72	7.65	−2.62	−2.43	−2.35	−2.84	−3.81
	IVC	0.98	0.99	1.00	0.99	1.03	7.83	8.55	8.78	7.66	7.74	−3.27	−2.17	−3.25	−2.42	−2.77
	HVC	0.98	0.99	1.00	0.99	1.03	7.84	8.46	8.61	7.64	7.27	−16.46	−8.71	−11.32	−6.00	−8.75
SPC	LVC	1.01	1.01	1.02	1.02	1.02	10.99	11.46	11.61	11.16	11.33	−0.24	−0.05	−0.48	−0.20	−0.33
	IVC	0.99	1.00	1.01	1.01	1.01	7.74	7.93	8.38	7.84	8.01	−5.82	−3.23	−1.95	−2.53	−3.36
	HVC	1.00	1.01	1.02	1.02	1.02	9.03	9.40	9.49	9.39	8.94	−1.92	−2.27	−3.50	0.48	5.22
SPIDER	LVC	0.99	1.00	1.02	0.97	1.03	10.59	10.55	11.45	10.61	10.81	0.09	−0.09	0.03	0.06	0.10
	IVC	0.98	0.99	1.01	0.96	1.02	7.94	8.49	8.80	8.23	8.37	0.19	−0.40	0.17	−0.41	−0.94
	HVC	0.93	0.94	0.96	0.91	0.96	7.57	7.87	7.98	7.69	7.51	−12.02	−10.42	−12.09	−10.06	−8.22
UMA	LVC	1.01	1.02	1.03	1.01	1.01	8.48	8.51	8.92	8.47	8.35	−0.21	−0.28	−0.12	0.03	−0.02
	IVC	1.00	1.02	1.03	1.00	1.00	7.69	8.24	8.29	7.98	7.43	−1.33	−0.86	−1.62	−2.00	−1.63
	HVC	1.00	1.02	1.03	1.00	1.01	8.05	8.57	8.49	8.26	7.58	0.23	−0.05	0.21	0.95	0.04
UMAEAST	LVC	1.00	1.01	1.01	0.99	1.02	6.43	6.73	6.95	6.28	6.32	−0.42	−0.13	−0.21	−0.24	0.11
	IVC	1.00	1.01	1.01	0.99	1.02	6.61	7.19	7.23	6.77	6.76	−0.35	−0.89	−0.73	−0.36	−0.71
	HVC	1.00	1.01	1.01	0.99	1.02	7.64	7.97	8.46	7.73	7.47	−0.72	−2.69	0.79	−3.52	−0.79

Notes. $\delta_\nu = \langle\delta\epsilon'_\nu\rangle/\delta\epsilon_\nu$ is the ratio of the average statistical uncertainty of the emissivities estimated in the fits of the simulated data to the statistical uncertainty estimated in the fit of the actual data. A second quantity, with the same denominator, $\phi_\nu = \sigma(\epsilon'_\nu)/\delta\epsilon_\nu$ is the ratio of the standard deviation of the emissivities recovered in the simulations to the statistical uncertainty estimated in the fit of the actual data. The percentage bias in emissivity $b_\nu = 100(\langle\epsilon'_\nu\rangle - \epsilon_\nu)/\epsilon_\nu$.

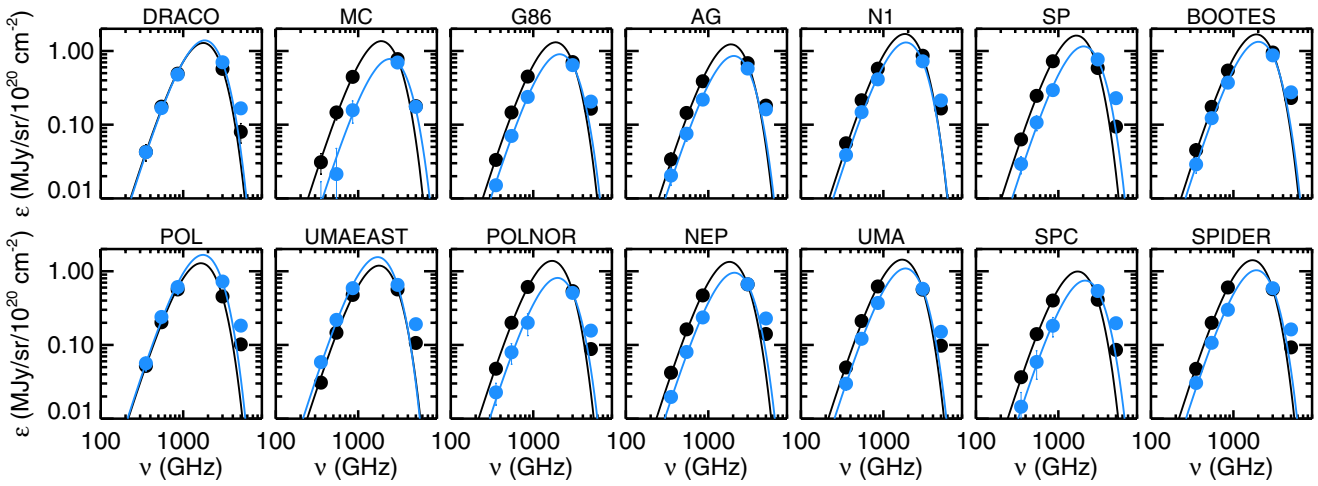

Fig. 16. SEDs from the emissivities of LVC (black) and IVC (blue) components for all the fields in our sample. For each H I component in each cloud, the solid line is the modified black body fit using 353, 545, 857, and 3000 GHz data.

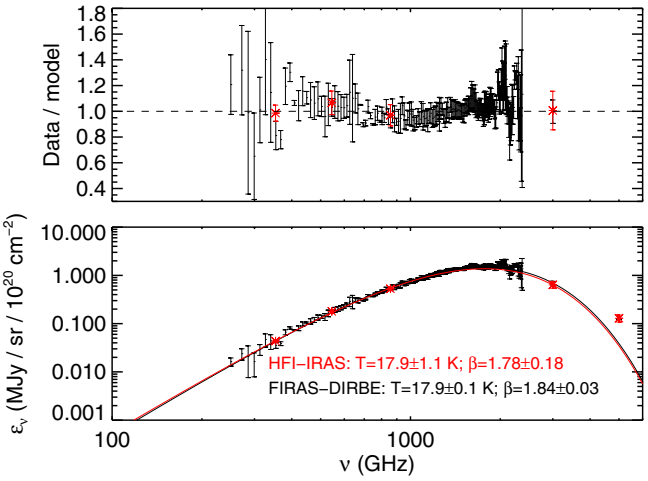

Fig. 17. *Bottom panel*: black points show the FIRAS spectrum of the diffuse ISM (Compiègne et al. 2011). The red points are the average of the IRAS or *Planck* emissivities for the local components of all our fields; the uncertainty is the variance of the values divided by $\sqrt{N}$. The solid curves are modified black body fits to each spectrum – the 5000 GHz point was excluded from the fit as it is dominated by non-equilibrium dust emission. *Top panel*: same as bottom panel but each data set is divided by its modified black body fit.

5.4. Dust properties

The modified black-body fit (Eq. (9)) provides information on the properties, such as T, of the dust in each H I component. A useful quantity used below is the emission cross-section of the interstellar material per H:

$$\sigma_e \equiv \kappa_0(\nu/\nu_0)^\beta \mu m_H = \tau/N_{HI}. \quad (10)$$

It is simply the prefactor to the Planck function in Eq. (9). In what follows we adopt $\nu_0 = 1200$ GHz ($\lambda_0 = 250\,\mu$m) to compare directly with the value of $\sigma_e(1200) = \tau/N_{HI}$ at 250 μm given by Boulanger et al. (1996).

A key quantity is the luminosity per H atom L (in W/H) emitted by dust grains (equal to the absorbed power) computed by integrating the SED over ν:

$$L = \int 4\pi\,\kappa_0(\nu/\nu_0)^\beta \mu m_H B_\nu(T)\,d\nu. \quad (11)$$

Complementing the actual SEDs in Fig. 16, Fig. 18 shows the derived values of $\sigma_e(1200)$, T and L plotted against the velocity of each H I component (LVC and IVC) in our sample.

The average emission cross-section for the 14 LVC components of our sample is $1.0 \pm 0.3 \times 10^{-25}$ cm^2, in good agreement with the value of 1×10^{-25} cm^2 obtained by Boulanger et al. (1996). The scatter of $\sigma_e(1200)$ for the LVCs (30%) is not the result of errors.

The emission cross-section for the IVC components is different, often 50% lower compared to the LVCs. There appear to be differences among the IVCs too, perhaps related to the fact that they belong to different IVC complexes. All fields in our sample overlap with the Intermediate Velocity (IV) Arch, except MC which is in the southern Galactic sky and belongs to the PP Arch and BOOTES which is part of Complex K (Kuntz & Danly 1996). The North Celestial Loop also overlaps spatially with the Low-Latitude Intermediate Velocity (LLIV) Arch (Kuntz & Danly 1996), an H I feature at slightly less negative velocity (~ -50 km s^{-1}) than the IV Arch (~ -75 km s^{-1}). The fields UMA and UMAEAST contain clumps identified by Kuntz & Danly (1996) as being part of the LLIV Arch (specifically LLIV1, LLIV2 and LLIV3). The field POL also contains emission that can be attributed to the LLIV Arch. These different complexes are identified with separate symbols in Fig. 18. The outliers are POL, UMAEAST (high) and MC (low). Excluding these $\sigma_e = 0.5 \pm 0.2 \times 10^{-25}$ cm^2 for the rest.

The values of T for the LVCs ($T = 17.9 \pm 0.9$ K) are in accordance with that obtained from the FIRAS spectrum at high Galactic latitude ($T = 17.9 \pm 0.1$ K; Fig. 17) and also close to the 17.5 K found by Boulanger et al. (1996) assuming $\beta = 2$. Like for σ_e, a systematic difference in T is found between LVCs and IVCs, even though it is less statistically significant. On average the IVC group of clouds[6] has $T = 20.0 \pm 1.0$ K, a value greater than in the local ISM at the 2.1σ level. Note the different IVC complexes as well.

Regarding L the striking result here is the small variation observed over all the fields and H I components. Combined together, the LVCs and IVCs have $\langle L \rangle = 3.4 \pm 0.6 \times 10^{-31}$ W/H, representing a variation of only 20% over all clouds. The fact that L is rather constant over all fields and H I components can also be appreciated in Fig. 16, where all SEDs are at about the same level. The small variation of L is surprising as it indicates

[6] Excluding POL, UMAEAST and MC.

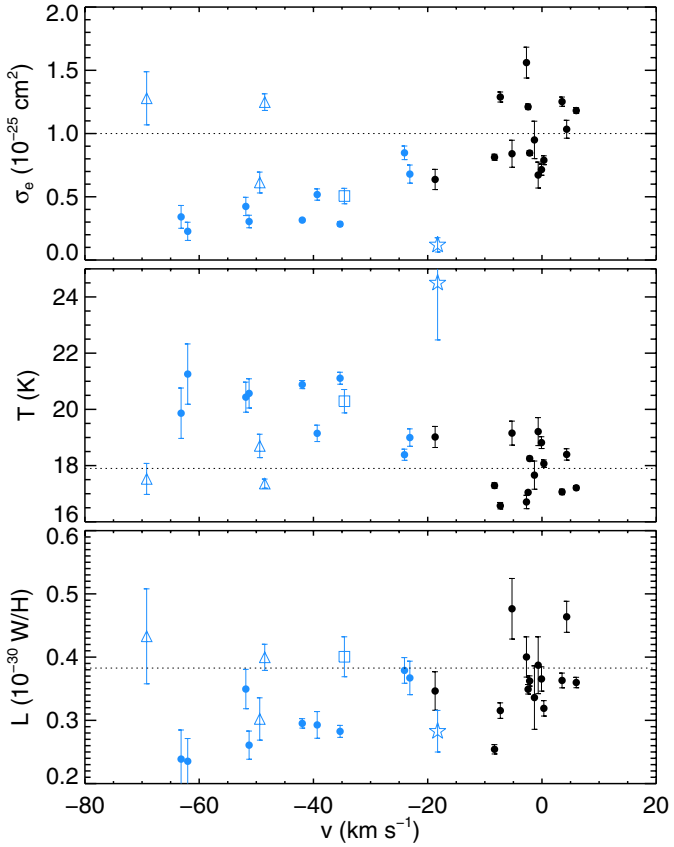

Fig. 18. Values of σ_e at 1200 GHz (250 μm), T and L versus the average velocity of each H I component. These dust parameters were estimated from the SED fit over the range 353 to 3000 GHz to a modified black body with $\beta = 1.8$. Black and blue symbols are for LVC and IVC, respectively. The different symbols in blue represent IVCs associated with specific complexes: IV Arch (dot), IV/LLIV Arch (triangle), Complex K (square) and PP Arch (star). In *each panel* the dotted line represent the value for the diffuse ISM obtained with the high-latitude FIRAS spectrum (see Fig. 17). Error bars are given for each data point, some being smaller than the symbol size.

that the power absorbed by dust is also rather constant, possibly suggesting constancy of the radiation field across all fields even at the distance of IVCs.

We have made the same analysis with a floating β to evaluate the robustness of the results shown in Fig. 18. The greatest impact of a floating β is on the uncertainty of T, and to a lesser degree on σ_e. The values of L are particularly insensitive because the modified black-body still serves effectively as an interpolation function between the measured data points. Even though the uncertainties on T and σ_e increase with a floating β, the trends seen in Fig. 18 are still observed, even more pronounced. We conclude that using $\beta = 1.8$ is a reasonable and conservative approach.

5.5. SED of the residual emission

As seen in Figs. 4 to 11, the residual emission once the H I model is subtracted from the *Planck* and IRAS maps exhibits significant spatial coherence which reproduces from frequency to frequency. In order to estimate the SED of this residual emission in each field, we carried out a linear regression analysis between the residual map at each frequency and the residual map at 857 GHz. The resulting slope of the regression (in units of MJy sr^{-1}/MJy sr^{-1} and equal to 1 at 857 GHz, by construction) can be used to estimate the shape of the spectrum of this residual emission. The results are presented in Fig. 19.

As for the SEDs of the H I-correlated emission, the SEDs of the residual are well fit by a modified black body function. We note a significant difference in the SED shape between low H I column density fields and brighter regions. The SEDs of brighter fields, where the residual emission is likely to come from molecular gas (Sect. 6.1), could be fit with $\beta = 1.8$ but with a slightly lower temperature ($T = 16.1 \pm 0.6$ K) than the LVC components. On the other hand, the SED of fainter fields, where the residual emission is most probably dominated by CIB anisotropies, could not be fit with $\beta = 1.8$. It is better described with $T = 18.6 \pm 0.9$ and $\beta = 1.1 \pm 0.1$. This should be taken only as a convenient fitting function, nothing physical. The significantly different value of β found here is probably the result of the complex composite nature of these fluctuations coming from the combination of all galaxies along the line of sight in slices of redshift which change with frequency (Planck Collaboration 2011n).

6. Discussion

6.1. The H I-H_2 transition

One possible contribution to the residual emission is dust associated with ionized gas. The WIM has a vertical column density of about 1×10^{20} cm^{-2} (Reynolds 1989; Gaensler et al. 2008), a significant fraction of the total column density in the most diffuse areas of the sky. Planck Collaboration (2011n) showed that, once the emission correlated with H I is removed from the *Planck* 353, 545 and 857 GHz data in faint fields, the residual emission has a power spectrum compatible with k^{-1}, much flatter than any interstellar emissions. We also showed that the amplitude of the residual in faint fields is constant from field to field (see Fig. 15), compatible with an isotropic extra-galactic emission. These are strong indications that dust emission associated with the WIM, and not correlated with H I, is small.

In the eight fields with bright cirrus, the residuals to the IR-H I correlation are skewed toward positive values, larger than the amplitude of the CIB fluctuations. The most straightforward interpretation is that these positive residuals trace dust emission within H_2 gas. This interpretation is reinforced by the fact that in the brightest fields (e.g., UMA, UMAEAST, and POL) we have checked that the residual emission is very well correlated with CO emission (Dame et al. 2001; Planck Collaboration 2011o), confirming the previous study of Reach et al. (1998) in the North Celestial Loop region (see their Fig. 11). The lower dust temperature estimated from the SED of the residual emission in all these bright fields (see Fig. 19) is also reminiscent of what is observed in molecular clouds (Planck Collaboration 2011u).

In the following we assume that the submm excess emission provides a way to estimate the molecular gas column density within the local ISM (LVC) component[7]. In order to estimate the fraction of H_2 in our fields we carried out an analysis using the I_{857} dust maps and the following equation explained below:

$$N_{\rm H}^{\rm LVC\prime} = \frac{I_{857} - \epsilon_{857}^{\rm IVC} N_{\rm HI}^{\rm IVC} - \epsilon_{857}^{\rm HVC} N_{\rm HI}^{\rm HVC} - Z_{857}}{\epsilon_{857}^{\rm LVC}}. \quad (12)$$

[7] This is not true for the DRACO field where the excess emission is likely to be dominated by Intermediate-Velocity gas which has accompanying CO emission (Herbstmeier et al. 1993). For this reason this field was discarded in the current analysis.

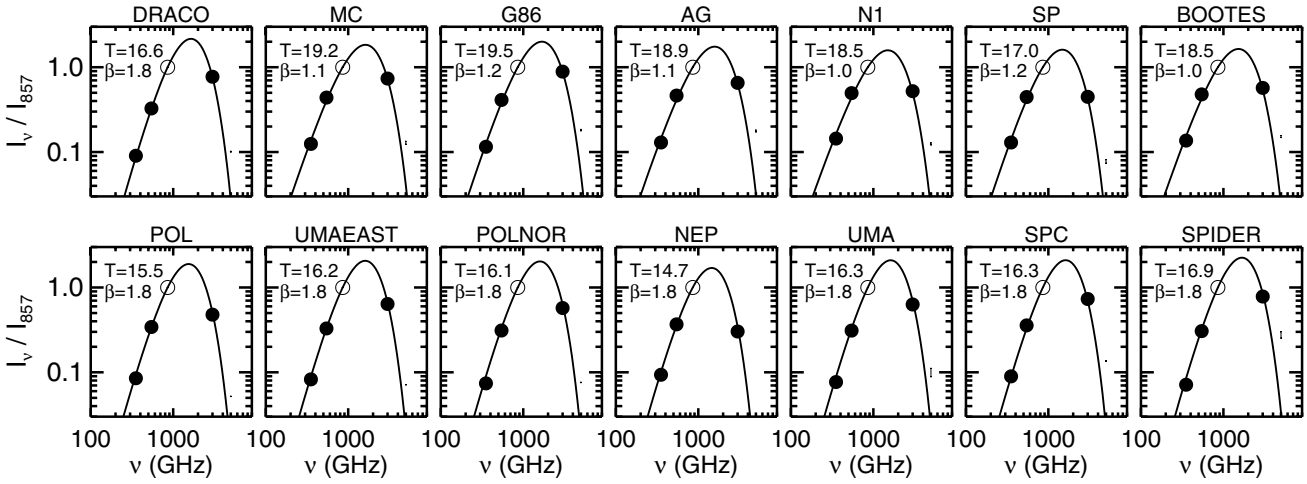

Fig. 19. Correlation coefficient of the residual emission with the 857 GHz residual. Similar to Fig. 16, the solid line here is the normalised modified black body SED fit using 3000, 545 and 353 GHz data. We assumed a fixed $\beta = 1.8$, except for the six most diffuse fields (MC, G86, AG, N1, SP and BOOTES) where the residual emission is dominated by the CIB fluctuations. In these fields $\beta = 1.8$, typical of diffuse Galactic dust emission, does not provide a good fit; these SEDs require a smaller value of β (see text).

To concentrate on the local (LVC) gas, we removed the IVC and HVC-correlated emission and the constant term from I_{857}, using the above results of the linear regression in each field. Assuming the dust emissivity is the same in the molecular gas as in the atomic gas from which it formed, we divided this by $\epsilon_{857}^{\rm LVC}$ for each field to produce estimated maps of the total column density $N_{\rm H}^{\rm LVC\prime}$ for the local/low-velocity gas. We note that this map still includes the fluctuations of the CIB (C_{857}) that act like a noise on the true total column density $N_{\rm H}^{\rm LVC}$:

$$N_{\rm H}^{\rm LVC\prime} = N_{\rm H}^{\rm LVC} + C_{857}/\epsilon_{857}^{\rm LVC}. \quad (13)$$

We of course have a map of the LVC atomic column density ($N_{\rm HI}^{\rm LVC}$) from the GBT measurements. Therefore, we are able to compute an estimate of the molecular column density map $N_{H2}^{\rm LVC} = (N_{\rm H}^{\rm LVC\prime} - N_{\rm HI}^{\rm LVC})/2$ and then calculate an estimate of the fraction of mass (or fraction of H nuclei) in molecular form, $f(\rm H_2) = 2\,N_{\rm H2}^{\rm LVC}/(2N_{\rm H2}^{\rm LVC} + N_{\rm HI}^{\rm LVC})$, pixel by pixel. The results obtained by combining all pixels in all fields, except DRACO, are plotted in Fig. 20. To produce this figure we binned the data in $N_{\rm H}^{\rm LVC\prime}$ and within each bin examined the PDF of $f(\rm H_2)$, finding its median (dark symbol) and half-power points (error bars, which are not necessarily symmetrical).

On this figure are also plotted estimates of $f(\rm H_2)$ using *FUSE* data by Gillmon et al. (2006); Wakker (2006) (squares – high-latitude lines of sight) and Rachford et al. (2009) (triangles – Galactic Plane lines of sight). The combination of these two datasets covers the column density range probed in our analysis.

The results plotted in Fig. 20 reveal an increase in $f(\rm H_2)$ beginning at $N_{\rm H}^{\rm LVC} \sim 3 \times 10^{20}\,\rm cm^{-2}$ and reaching 0.8 for $N_{\rm H} \sim 4 \times 10^{21}\,\rm cm^{-2}$. Note that we are not sensitive to the much lower values of $f(\rm H_2)$ found by *FUSE* at low column densities. For pixels with $N_{\rm H}^{\rm LVC} < 3 \times 10^{20}\,\rm cm^{-2}$ the dispersion of our estimate of $f(\rm H_2)$ is due to the fluctuations of the CIB. For these pixels, $N_{\rm H}^{\rm LVC} \approx N_{\rm HI}^{\rm LVC}$ and therefore $N_{\rm H2}^{\rm LVC} \approx C_{857}/2\,\epsilon_{857}^{\rm LVC}$. Because C_{857} has a mean of zero, it produces both positive and negative values of $f(\rm H_2)$.

Note that the UV observations toward O stars in the Galactic Plane (triangles) give some $f(\rm H_2)$ values at the same level as we find, but also some much lower values for a given column density. This suggests that the UV observations are somewhat affected by clumpiness and/or are sampling qualitatively different lines of sight than ours at high latitude. Indeed Wakker (2006) emphasized that it is not straightforward to relate the H I-$\rm H_2$ transition to physical properties of the interstellar gas, like density in the molecule-producing environment, or even a physical threshold in column density required for molecule formation, because of the summing over different environments along the line of sight. A corollary is that there can be quite different values of $f(\rm H_2)$ for the same $N_{\rm H}$, as is seen in the figure, and so

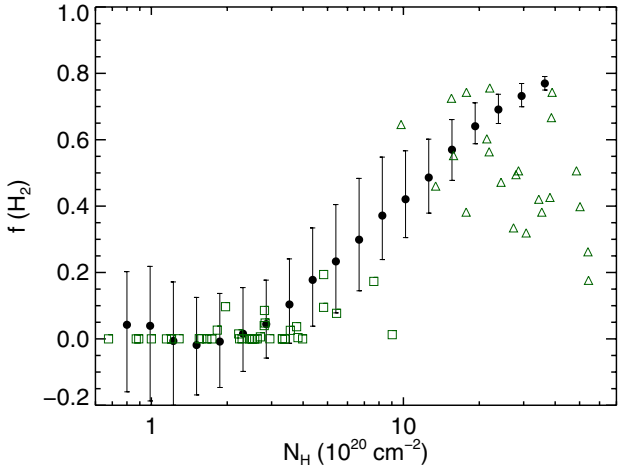

Fig. 20. Fraction $f(\rm H_2)$ of hydrogen that is in molecular form in local gas/LVC, calculated from emission excess relative to the linear correlation (see text), versus the total column density estimated using the 857 GHz dust emission transformed into gas column density using the emissivities ϵ_ν. Black points show the median value of $f(\rm H_2)$ in bins of $N_{\rm H}$ computed using all lines of sight in our sample. The error bars show the half-width at half maximum of the PDF computed in each $N_{\rm H}$ bin. Green symbols show the results obtained using UV absorption data from high-latitude surveys (Gillmon et al. 2006; Wakker 2006, squares) and toward O stars on lines of sight closer to the Galactic Plane (Rachford et al. 2002, 2009, triangles).

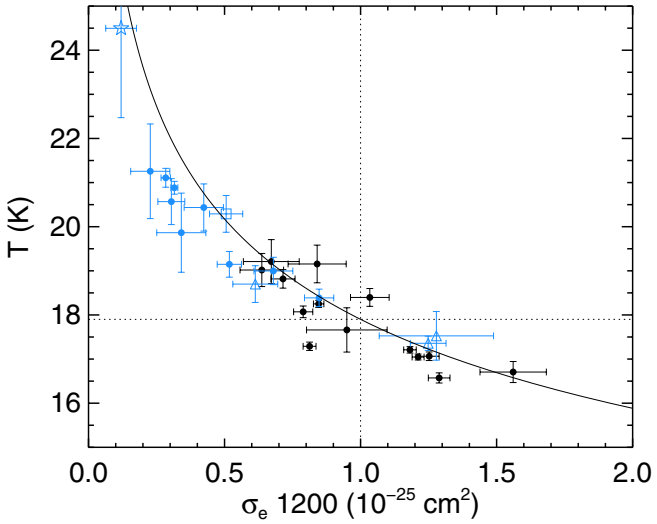

Fig. 21. Temperature vs emission cross-section at 1200 GHz (250 μm) estimated from modified black-body fit with $\beta = 1.8$ to data from 353 to 3000 GHz. Black is for LVCs, blue IVCs: IV Arch (dot), IV/LLIV Arch (triangle), Complex K (square) and PP Arch (star). The solid line respresents a constant emitted luminosity L corresponding to the diffuse ISM reference values ($\sigma_e = 1 \times 10^{-25}$ cm^{-2} and $T = 17.9$ K – dotted lines).

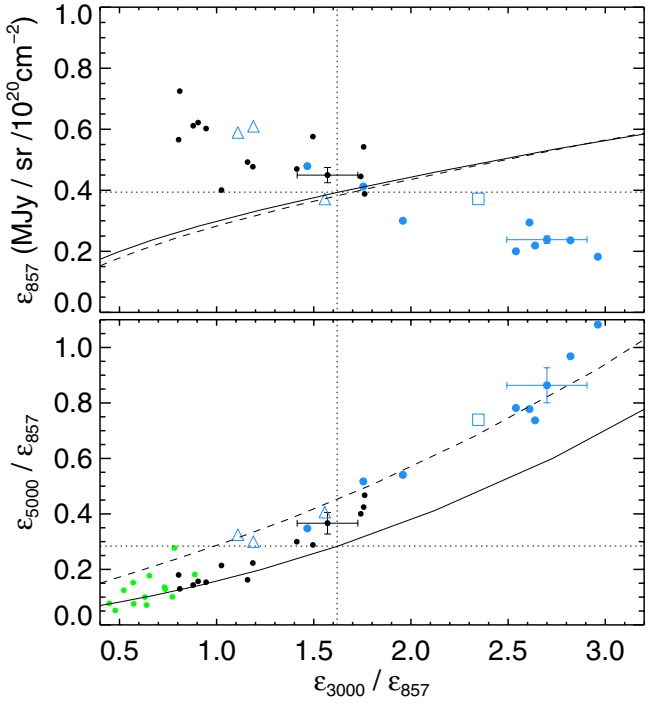

Fig. 22. *Top*: dust emission per N_{HI} at 857 GHz versus the 3000/857 GHz (100/350 μm) ratio. Local (black), IVC (blue – dot is IV Arch, triangle IV/LLIV Arch, square Complex K), residual (green). Solid line is the DustEM model for the diffuse ISM (Compiègne et al. 2011), with radiation field variations from $G = 0.1$ to $G = 5$. Dashed line is the same model but with a *relative* abundance of VSGs four times higher than the standard diffuse ISM value. Dotted lines gives the local ISM fiducial values ($G = 1.0$). Typical uncertainties are shown for each H I component. *Bottom*: 5000/857 GHz (60/350 μm) ratio as a function of the 3000/857 GHz (100/350 μm) ratio.

comparison of UV data with the complementary infrared/submm analysis is of great interest.

The overall correspondance between the trends seen independently in the *Planck* and *FUSE* results supports our interpretation of the submm excess being caused by dust associated with molecular hydrogen. We would call this medium "dark gas" if it were not detected via CO (Planck Collaboration 2011o). Although there are lines of sight where $f(H_2)$ is quite high, summed over all lines of sight in our survey, our study shows that the excess emission at 857 GHz that is not correlated with H I is only 10% of the total emission. Thus the fraction of the hydrogen gas mass that is in molecular form in this sample of the high latitude diffuse interstellar medium in the solar neighbourhood is quite low. Planck Collaboration (2011o) estimated a value of 35% for the entire high-latitude sky above 15°, which includes higher column density lines of sight (this introduces yet another factor, H I self-absorption, to make the medium dark). Of this 35%, about half is traced by CO, leaving about 20% as "dark gas" not traced by CO or H I.

The structure and nature of the diffuse molecular gas can be studied using the maps of residual (excess) dust emission. In SPIDER (see Fig. 9), an intermediate column density field where there is very little CO emission detected (Barriault et al. 2010), we observe coherent filamentary structures in the residual map that we interpret as the presence of dust in diffuse H_2 gas without CO. We have checked that the structures cannot be accounted for by an underestimate of the 21-cm line opacity correction, being present even with T_{spin} as low as 40 K. In this field the submm residual provides a way to map the first steps of the formation of molecules in the diffuse ISM.

6.2. Evolution of dust

6.2.1. Variations of the big grain emission cross-section

Interstellar dust evolves through grain-grain and gas-grain interactions. Fragmentation and coagulation of dust grains are expected to occur in the ISM, modifying not only the grain size distribution but also the grain structure. The data described here provide important evidence for dust processing in diffuse local clouds and IVCs. As we will elucidate, the evidence foreshadowed in Fig. 18 can be seen in Figs. 21 and 22.

Figure 21 shows the values of T and $\sigma_e(1200)$ already shown in Fig. 18 but here as a scatter plot. The solid line shows the expected $\sigma_e(1200)$ as a function of T for a constant emitted luminosity L (normalized to 3.8×10^{-31} W/H, the average diffuse ISM values for $T = 17.9$ K and $\sigma_e(1200) = 1.0 \times 10^{-25}$ cm^{-2}).

The emission cross-section σ_e reflects the efficiency of thermal dust emission per unit mass. Dust that emits more efficiently will have a lower equilibrium temperature, the trend seen. Note that the dust in very different environments has close to the same integrated emission (L) and therefore is absorbing about the same power (solid line). The comparison with the values found in the Taurus molecular cloud by Planck Collaboration (2011u) ($T \sim 14.5$ K, $\beta = 1.8$, $\sigma_e \sim 2.0 \times 10^{-25}$ cm^{-2} and $L = 2.3 \times 10^{-31}$ W/H) suggests that the $T - \sigma_e$ anti-correlation extends to colder dust and denser environments, although the typical power absorbed is lower because of shielding.

Because σ_e depends only on the dust properties and on the dust-to-gas ratio, the 30% variation observed in local ISM (LVC – see Fig. 18), where we expect little variations of the metallicity, is interpreted as a genuine variation of the dust properties from one cloud to another. An alternative explanation would be the presence of different amounts of H_2 gas spatially correlated

with the H I. In this case the dust opacity $\sigma_e(1200)$ would be overestimated due to an underestimate of the actual gas column density. Although this scenario cannot be excluded formally, the data shown here does not support an increase of $\sigma_e(1200)$ with N_{HI} through the H I-H_2 transition, as one might expect in this case. For this reason we favor an interpretation of the variations of $\sigma_e(1200)$ related to modifications of the grain properties.

Figure 22 complements Fig. 21 by comparing directly measured emissivities (ϵ_ν) with the DustEM model of the average diffuse high latitude emission. This comparison, independent of any modified black-body fit, also shows strong evidence for dust evolution. The top plot of Fig. 22 shows the 857 GHz emissivity versus the 3000 GHz to 857 GHz ratio. This is compared to a simple DustEM model prediction for constant dust properties and a variation of the radiation field strength from $G = 0.1$ to $G = 5$ ($G = 1$ being the fiducial value). The prediction of DustEM is an increase of both ϵ_{857} and $\epsilon_{3000}/\epsilon_{857}$ with increasing radiation field strength, and therefore T. The former increases with G simply because of the increase of $B_\nu(T)$. The ratio $\epsilon_{3000}/\epsilon_{857}$ increases with T as the peak of the black-body shifts towards higher frequencies. The data points do not follow this trend showing clearly that the variations in the SEDs found here in LVCs and IVCs cannot be explained by local variations of the radiation field strength. The data are consistent with a decrease of the dust emission cross-section ($\sim\epsilon_{857}$) with temperature ($\sim\epsilon_{3000}/\epsilon_{857}$), the same trend seen in Fig. 21. An evolutionary model in which dust structure changes due to aggregation (and the reverse process, fragmentation) is qualitatively consistent with these results: grains with a fluffy structure will absorb about the same amount of optical and ultraviolet radiation per unit mass as more compact grains, but compared to these more homogeneous and spherical grains they are more emissive at submm wavelengths because of their more complex structure and therefore cool more efficiently (Stepnik et al. 2003).

6.2.2. Dust shattering in Intermediate Velocity clouds?

The bottom plot of Fig. 22 shows the 5000 GHz to 857 GHz emissivity ratio as a function of the 3000 GHz to 857 GHz ratio for all H I components and the residual emission SEDs. The locus from standard ISM DustEM models shows an effect of increasing colours with increasing G. The bright cirrus clouds of the LVC components (black symbols at the left end of the plot) and the molecular residuals (green) have colours in good agreement with the standard DustEM model, consistent with some variation of $G \lesssim 1$.

Both ratios are higher for the IVCs and the trend is offset relative to the standard locus. The qualitative interpretation is that the emission in these higher-frequency bands is more contaminated by non-equilibrium emission from an increased relative abundance of very small grains (VSGs) compared to the larger grains (BGs) in thermal equilibrium. To make this more quantitative, the dashed curve passing closer to the IVC data shows the colours for a DustEM diffuse ISM model with a *relative* abundance of VSGs four times higher than the standard value.

Because of their non-equilibrium emission, VSGs dominate the emission for $\nu > 5000$ GHz and, according to the standard DustEM model and for the standard radiation field ($G = 1$), contribute to 30% of the emission in the IRAS 60 μm band even with an abundance of only 1.6% of the total dust mass. By contrast, the BGs make up 90.7% of the total dust mass, 14.2% carbon rich and 76.5% silicates. Therefore an increase of a factor four of the mass in VSGs is easy to accommodate by shattering of a small fraction of the BG dust mass. The fact that the emission cross-section of IVCs is a factor of two lower than for the local ISM can be due to a decrease of the mass in BGs (i.e., the dust-to-gas mass ratio) and/or to a decrease in the emission cross-section of a single grain, the latter affecting the equilibrium dust temperature. For the average temperature found in IVC_b ($T = 20.4$ K), and considering a variation of the dust-to-gas mass ratio from 1 to 1/2 the local ISM value, the radiation field strength needed to explain these results would be $G = 1-2$, not an unreasonable range for IVCs. It is thus difficult to conclude at this point on the exact nature of the variation of σ_e in IVCs. On the other hand these results are clearly compatible with a modification of the BGs (total mass and/or grain properties) and a significant increase of the abundance of VSGs. The details would be linked to the specific dynamical and shock history of this interstellar matter that is part of the Galactic fountain (Shapiro & Field 1976; Houck & Bregman 1990).

6.3. Dust in high-velocity clouds

Dust emission in HVCs is expected to be weak for several reasons. First, their great distance from the Galactic disk (typically several kpc – Wakker 2001; van Woerden & Wakker 2004) implies a faint radiation field, hence a low dust equilibrium temperature and a low luminosity (Wakker & Boulanger 1986; Trifalenkov 1993; Miville-Deschênes et al. 2005). But the main reason comes from gas phase abundance measurements obtained from absorption lines of oxygen, silicon and iron in the far-UV. Because oxygen is mostly in the gas phase and because its ionization potential is similar to hydrogen, the ratio O I/H I provides the most robust measure of metallicity in diffuse clouds. Unlike oxygen, iron and silicon are depleted into dust grains in the local ISM (Savage & Sembach 1996); low ratios of Si/O and Fe/O thus trace the presence of dust. In most HVCs the O I/H I ratio shows that the metallicity is significantly sub-solar (of the order 0.1–0.5 solar, see Lu et al. 1998; Wakker et al. 1999; Richter et al. 2001; Tripp et al. 2003; Sembach et al. 2004; van Woerden & Wakker 2004; Fox et al. 2006; Collins et al. 2007), indicative of their extragalactic origin. In addition the Si/O and Fe/O ratios in Complex C are infered to be close to solar (Richter et al. 2001; Collins et al. 2007) indicating little silicon and iron locked in dust grains. Together the overall low abundance of metals and the fact that Si and Fe seem to be mostly in the gas phase imply a low dust to gas ratio in HVCs.

Nevertheless, because of the unknown enrichment history of HVCs that might set different intrinsic abundances than in the solar sytem[8], the difficulty to estimate the effect of ionization on Si II and Fe II to infer the abundances of Si and Fe[9], and the unkown nature of dust in HVCs[10], the link between the metallicity, the depletions and the amount of dust remains indicative. One illustrative related example, albeit for an IVC, is the finding by Richter et al. (2001) of only mild depletion of Si and Fe for the IVC IV-Arch which nevertheless has dust emission at a comparable level to the local ISM. Thus the search for dust emission from HVCs is an interesting complementary way to put contraints on the physical conditions and nature of matter in the Galactic halo.

[8] O and Si are mostly produced in Type II supernovae, Fe is produced primarly in Type Ia supernovae.

[9] The true abundance of Si and Fe are less than the ones infered from Si II/H I and Fe II/H I. To take this bias into account, an ionization correction is applied (Collins et al. 2003) that depends on gas density and radiation field strength, both not well constrained.

[10] The amount of carbonaceous dust is not constrained by gas phase abundances.

Table 5. Upper limit for the HVC emissivities in each field.

	ϵ_{353}	ϵ_{545}	ϵ_{857}	ϵ_{3000}	ϵ_{5000}
AG	<0.010	<0.029	<0.055	<0.071	<0.024
BOOTES	<0.079	<0.258	<0.519	<0.289	<0.106
DRACO	<0.021	<0.075	<0.168	<0.194	<0.054
G86	<0.035	<0.096	<0.232	<0.342	<0.087
MC	<0.003	<0.009	<0.017	<0.027	<0.037
N1	<0.016	<0.047	<0.094	<0.054	<0.018
NEP	<0.014	<0.040	<0.084	<0.085	<0.076
SP	<0.015	<0.041	<0.068	<0.040	<0.015
SPC	<0.012	<0.040	<0.090	<0.060	<0.030
SPIDER	<0.017	<0.061	<0.144	<0.113	<0.054
UMA	<0.007	<0.021	<0.056	<0.053	<0.024
UMAEAST	<0.017	<0.054	<0.135	<0.105	<0.028
LVC	0.045 ± 0.006	0.18 ± 0.03	0.52 ± 0.09	0.55 ± 0.10	0.10 ± 0.02
IVC	0.023 ± 0.015	0.09 ± 0.04	0.27 ± 0.09	0.66 ± 0.06	0.20 ± 0.03
HVC	<0.013	<0.040	<0.085	<0.077	<0.034

Notes. For the emissivities of the LVC and IVC components, weighted average and standard deviation of the 14 fields. Last row: average HVC upper limit, excluding BOOTES, G86 and SPIDER for which the H I column density of the HVC is less than 10^{19} cm^{-2} inside the mask. All values are in MJy sr^{-1}/10^{20} cm^{-2}.

After unsuccesful attemps to detect dust emission from HVCs using IRAS data (Wakker & Boulanger 1986; Fong et al. 1987; Bates et al. 1988; Désert et al. 1988), Miville-Deschênes et al. (2005) claimed a detection in Complex C using a combination of *Spitzer*, *IRAS* and GBT data. Compared to these previous searches, the analysis presented here extend greatly the number of fields, the surface covered and the wavelength coverage. The fields used here overlap with four HVC complexes: Complex C (DRACO, G86, N1, NEP, SP, SPIDER, BOOTES[11]), Complex M (AG), Complex A (SPC, UMA, UMAEAST) and the Magellanic Stream (MC). HVC-correlated emission is not detected significantly in any of these fields.

At each frequency the emissivities found are compatible with zero within 3σ, with about as many negative as positive values. At first glance, examination of the emissivities in Table 2 shows systematic behaviour across frequencies that could be taken as encouraging evidence for an HVC detection in some fields, like AG. However, this does not necessarily bolster the statistical significance of the detection in a single pass band. This is because the dust emission is intrinsically highly correlated frequency to frequency, as is the CIB, and so given the generally small noise, the fits to the correlations with (the same) $N_{\rm HI}$ are to first order just scaled versions of each other. This analysis establishes the main difficulties hampering the detection of dust emission from HVCs, the contaminating foreground emission of LVCs and IVCs and the background CIB fluctuations which greatly increase the uncertainties in $\epsilon_\nu^{\rm HVC}$ (Sect. 4.5 and Table 4).

In Table 5 we focus on the upper limits to the HVC emissivities. They were computed using a Bayesian approach in the case of Gaussian errors with a bounded physical region (Feldman & Cousins 1998); we assumed that the true emissivities can only be zero or positive. Table 5 gives the value of ϵ_ν for which there is 99.87% probability (equivalent to a 3σ upper limit) that the true emissivity is $\leq\epsilon_\nu$. These upper limits are compared in Table 5 to the weighted average of the measured emissivites for the LVC and IVC components; any dust in HVCs has an emissivity, on average, no more than 15% of the value found in the local ISM at 857 and 3000 GHz.

We considered the null hypothesis that the HVC emissivity is zero (or a small uniform value) in all fields and find that, at any given frequency, the weighted standard deviation of the measured HVC emissivities ($\sigma(\epsilon)$) is somewhat larger than expected given the uncertainties on each measurement. This is true even when considering only AG, N1, MC and SP, the fields with significant HVC H I column density and almost no masking. For example, the probability of obtaining the measured $\sigma(\epsilon)$ is only 0.2% at 857 GHz for these four fields. One explanation could be that we have underestimated the uncertainties on each measurement; to increase the probability of the measured $\sigma(\epsilon)$ to 10% at 857 GHz, the uncertainties would need to be multiplied by 1.6. But even such a moderate increase of the uncertainties seems unlikely in the most diffuse fields considered here because the noise is dominated by the strongly constrained and well modeled CIB fluctuations (Planck Collaboration 2011n). A second explanation is that the $\sigma(\epsilon)$ reflects a variation of the true ϵ from field to field. For these four fields we verified that, if one allows for a variation of ϵ from field to field following a uniform distribution in the range between zero and the upper limit of each field, the probability of obtaining the measured $\sigma(\epsilon)$ reaches 15% at 857 GHz without having to increase the uncertainties on the individual measurements. If this is the right explanation, the measured value of $\sigma(\epsilon)$ implies that ϵ is small but non-zero in some fields.

Finally, there have been many interesting discussions of the possible relationships between IVCs and HVCs (e.g., Albert & Danly 2004; Wakker 2001). Here the relative emissivity is of some relevance; as our data show, H I-correlated emission is readily detected in IVCs, but not in HVCs. A specific example is provided by our AG field which encompasses the cloud MI in HVC Complex M (Wakker 2001). The low HVC emissivity in contrast to the fairly normal IVC emissivity (Table 2) does not support any direct relationship between MI and the intermediate velocity gas in the IV Arch in this direction (Wakker 2001).

7. Conclusions

We have presented results of a first comparison of *Planck* and IRAS with new H I 21-cm line GBT data for 14 high Galactic latitudes fields, covering about 825 deg^2 on the sky. Using the velocity information of the 21-cm data we made column density maps of the LVC, IVC, and HVC in each field. By correlating these H I maps with the submm/infrared dust emission maps

[11] BOOTES is on the side of Complex C. It has faint emission from –80 to –100 km s^{-1} that could also be associated with the IVC Complex K.

we estimated the distinct dust emissivities for these three high-latitude components and made corresponding SEDs from 353 to 5000 GHz.

On average, the dust SED of the local ISM (LVC) deduced from the IRAS and *Planck* data is compatible with that from the FIRAS data over the high-latitude sky and is well fit with a modified black body with parameters $\beta = 1.8$ and $T = 17.9$ K. On the other hand, even though the energy emitted by dust is rather constant in our sample, we report significant variations of the dust SED shape, compatible with variations of the dust temperature anti-correlated with the emission cross-section. We interpret these variations as a signature of active evolution of the dust grain structure through coagulation and fragmentation in the diffuse ISM.

For faint cirrus fields with average H I column density lower than 2×10^{20} cm^{-2}, the residual FIR-submm emission, after removal of the H I-correlated contributions, is normally distributed with a standard deviation compatible with the expected level of CIB fluctuations. The SED of the residual is unlike any interstellar component. For such diffuse fields we also show that the interstellar dust emission is dominated by the contribution from atomic gas.

For fields with larger H I column density there are significant FIR-submm emission excesses that, for the brightest fields, follow the structure of the CO emission. For intermediate column density regions, the residual emission shows coherent spatial structures not seen in CO, revealing the presence of H_2 gas. The SED of this residual shows that it is slightly colder than the dust in the local H I. There is a lot of variation in $f(H_2)$, the fractional mass in the form of H_2, but over the whole survey of these diffuse fields the fraction is only 10%.

We report strong detection of dust emission from all IVCs in our sample. The dust emission cross-section is typically two times lower than for the local ISM and the relative abundance of small grains having non-equilibrium emission is about four times higher than normal. This evolution of the dust properties is indicative of dust shattering in halo gas with the dynamics of a Galactic fountain. We also find that, compared to the local ISM, several of these clouds have a higher dust temperature which could also be the result of globally smaller grains. The total energy emitted by dust in IVCs is comparable to what is observed in the local ISM suggesting similar radiation field strength.

Finally, we have attempted to detect HVC-correlated dust emission. We show why this is very challenging, because of the uncertainties induced by foreground contamination and the CIB anisotropies. The average of the 99.9% confidence upper limits on the emissivity, 0.15 times the average emissivity found in the local ISM at 857 and 3000 GHz, is compatible with the low level of dust emission expected from HVCs based on their low metallicity and relatively low depletion of elements like Si and Fe.

Acknowledgements. A description of the Planck Collaboration and a list of its members can be found at http://www.rssd.esa.int/index.php?project=PLANCK&page=Planck_Collaboration. We thank the anonymous referee for many helpful comments.

Appendix A: Noise of the H I components

The analysis presented here relies on a correlation between far-infrared/submm data and the H I components deduced from 21-cm emission. In order to estimate properly the uncertainties on the correlation coefficients the noise on the H I components needs to be evaluated. We have made this estimate using two different methods which address different contributions to the noise (see Boothroyd et al. 2011).

First we applied the traditional method in which the end channels of the 21-cm spectrum, where there is no emission. The velocity channels are independent, i.e., the spectrometer resolution is better than the 0.8 km s^{-1} channel width. A large number of end channels can be used to compute a map of the standard deviation of the noise at each (x, y) position:

$$\delta_{Tb}(x,y) = \sqrt{\frac{1}{N_\delta - 1}\sum_{v=v1}^{v2} T_b^2(x,y,v) - \frac{1}{N_\delta}\left(\sum_{v=v1}^{v2} T_b(x,y,v)\right)^2}, \quad \text{(A.1)}$$

where $N_\delta = v2 - v1 + 1$ is of the order of 200 channels. For the GBT data, this is a very flat map, whose typical value is the same as the standard deviation of a single end channel. This is about 0.17 K for a single visit to a field. Some fields were mapped two or three times.

The uncertainty map $\delta N_{\rm HI}(x,y)$ for the column density of a given H I component summed over N channels is

$$\delta N_{\rm HI}(x,y)\ [{\rm cm}^{-2}] = A\sqrt{N}\delta_{Tb}(x,y)\Delta v, \quad \text{(A.2)}$$

where Δv is the channel width in km s^{-1}. For $N \sim 60$, this amounts to $\delta N_{\rm HI} \sim 0.02 \times 10^{20}$ cm^{-2} for a single visit. This assumes, as is usual, that the noise properties estimated using the end channels are representative of the noise in channels summed to build the column density maps. Actually, the channel noise scales as roughly $(1 + T_b/20{\rm K})$ and this can be taken into account.

We developed a second method which exploits the fact that the H I brightness-temperature cubes were built by averaging independent data taken in different polarisations (called *XX* and *YY*). Each polarisation observation can be reduced separately, which requires separate baseline estimates for the spectra in the *XX* and *YY* cubes. Baseline fitting is another source of error. Taking the difference between the *XX* and *YY* cubes removes the common unpolarized H I emission, leaving in each velocity channel only the thermal noise and systematic effects from the baseline subtraction. The difference cube is

$$\Delta(x,y,v) = (T_{XX}(x,y,v) - T_{YY}(x,y,v))/2, \quad \text{(A.3)}$$

where we divide by two to give the same statistics as in the average of the cubes.

We make a map of the column density differences (divided by two) over the same channel range as for $N_{\rm HI}$:

$$\Delta N_{\rm HI}(x,y) = A\,\Delta v \sum_{v=v1}^{v2} \Delta(x,y,v). \quad \text{(A.4)}$$

The estimate of $\delta N_{\rm HI}$ is then the standard deviation of this map.

This method gives an uncertainty typically 1.3 times the simple estimate using end channels (it can reach up to 2 times for the brightest components) because it includes baseline uncertainties and the increase of thermal noise with signal. The column density uncertainties evaluated with this second method for each component in each field are given in Table 1). There are additional errors from the stray radiation correction that can affect the local and IVC components. The total uncertainty including this additional contribution can be estimated in a similar way to the second method if there are two or more visits to compare (Boothroyd et al. 2011). Because in cases with multiple visits these are found to be not much larger, and because the uncertainties in $N_{\rm HI}$ are not the major source of uncertainty in the correlation analysis (Sect. 4.5), adopting the values in Table 1 is satisfactory for our purposes.

Table B.1. *Planck* and IRAS noise levels (in MJy sr^{-1}) for each field and at each frequency.

Field	σ_{353}	σ_{545}	σ_{857}	σ_{3000}	σ_{5000}
AG	0.0055	0.0095	0.0094	0.0295	0.0156
BOOTES	0.0078	0.0122	0.0124	0.0243	0.0156
DRACO	0.0044	0.0075	0.0073	0.0234	0.0115
G86	0.0056	0.0085	0.0086	0.0243	0.0147
MC	0.0088	0.0140	0.0139	0.0306	0.0172
N1	0.0050	0.0084	0.0083	0.0218	0.0120
NEP	0.0040	0.0065	0.0063	0.0265	0.0138
POL	0.0061	0.0095	0.0098	0.0333	0.0141
POLNOR	0.0054	0.0087	0.0088	0.0252	0.0134
SP	0.0055	0.0086	0.0088	0.0268	0.0153
SPC	0.0065	0.0104	0.0104	0.0280	0.0142
SPIDER	0.0058	0.0093	0.0096	0.0277	0.0143
UMA	0.0065	0.0101	0.0108	0.0340	0.0156
UMAEAST	0.0072	0.0111	0.0113	0.0365	0.0167

Notes. The value given here is the noise level in the map that has been convolved to the 9.4′ GBT resolution.

Appendix B: Estimating the noise of the *Planck* and IRAS maps

To estimate the noise level of the IRAS and *Planck* maps we use the difference between independent observations of the same sky. For IRAS, the original ISSA plates (Wheelock et al. 1993) were delivered with three independent set of observations (called HCONs), each obtained at different periods during the life of the satellite. Each HCON has its own coverage map. The ISSA final product is the coverage-weighted co-addition of the three HCONs. The IRIS product (Miville-Deschênes & Lagache 2005) also contains the three HCONs.

A similar approach was used to estimate the noise of each *Planck* map. For each pointing period *Planck* scans the sky about 50 times. The Data Processing Centre delivered two maps made with data from the first half and second half of each pointing period, respectively. In this case the number of samples used to estimate the signal at a given sky position is the same in the two maps (i.e., the coverage map is identical for the two maps). Again we used the difference between these two maps of the same region of the sky to estimate the noise.

Here we want to estimate the average noise level δI_ν of an IRAS or *Planck* map I_ν used for the analysis given a difference map

$$\Delta_\nu(x,y) = (I_{\nu,1}(x,y) - I_{\nu,2}(x,y))/2 \tag{B.1}$$

obtained from independent observations, each $I_{\nu,i}$ map having its own coverage map $N_{\nu,i}$. In the general case (Miville-Deschênes & Lagache 2005), δI_ν is obtained by taking the standard deviation of the map

$$\Delta'_\nu(x,y) = \Delta_\nu(x,y)\sqrt{\frac{4\,N_{\nu,1}(x,y)\,N_{\nu,2}(x,y)}{N_\nu(x,y)\,(N_{\nu,1}(x,y)+N_{\nu,2}(x,y)}}. \tag{B.2}$$

In the case of *Planck*, $N_{\nu,1} = N_{\nu,2} = N_\nu/2$ and so $\Delta'_\nu = \Delta_\nu$ and the standard deviation of the average map is the same for the difference map, as expected. Because the ISSA plates are the combination of three observations with different coverages such a simplification is not possible and the above more general equation has to be used.

In our analysis we used the IRAS and *Planck* maps convolved to the 9.4′ resolution of the GBT. Therefore, the appropriate δI_ν is obtained by first convolving the $\Delta'_\nu(x,y)$ map and then taking the standard deviation. These are the noise levels tabulated for each field in Table B.1.

References

Albert, C. E., & Danly, L. 2004, in High Velocity Clouds, ed. H. van Woerden, B. P. Wakker, U. J. Schwarz, & K. S. de Boer, 312, 73
Arendt, R. G., Odegard, N., Weiland, J. L., et al. 1998, ApJ, 508, 74
Barriault, L., Joncas, G., Falgarone, E., et al. 2010, MNRAS, 406, 2713
Bates, B., Catney, M. G., & Keenan, F. P. 1988, Ap&SS, 146, 195
Bersanelli, M., Mandolesi, N., Butler, R. C., et al. 2010, A&A, 520, A4
Blagrave, K., Lockman, F. J., & Martin, P. G. 2010, in The Dynamic Interstellar Medium: A Celebration of the Canadian Galactic Plane Survey, ed. A. G. W. R. Kothes, & T. L. Landecker, ASP Conf. Ser., 438, 156
Boothroyd, A., Blagrave, K., Lockman, F., Martin, P., et al. 2011, A&A, in press, DOI: 10.1051/0004-6361/201117656
Boulanger, F., & Pérault, M. 1988, ApJ, 330, 964
Boulanger, F., Abergel, A., Bernard, J., et al. 1996, A&A, 312, 256
Calabretta, M. R., & Greisen, E. W. 2002, A&A, 395, 1077
Collins, J. A., Shull, J. M., & Giroux, M. L. 2003, ApJ, 585, 336
Collins, J. A., Shull, J. M., & Giroux, M. L. 2007, ApJ, 657, 271
Compiègne, M., Verstraete, L., Jones, A., et al. 2011, A&A, 525, A103
Dame, T. M., Hartmann, D., & Thaddeus, P. 2001, ApJ, 547, 792
Désert, F., Macías-Pérez, J. F., Mayet, F., et al. 2008, A&A, 481, 411
Désert, F. X., Bazell, D., & Boulanger, F. 1988, ApJ, 334, 815
Dupac, X., Bernard, J., Boudet, N., et al. 2003, A&A, 404, L11
Feldman, G. J., & Cousins, R. D. 1998, Phys. Rev. D, 57, 3873
Field, G. B. 1965, ApJ, 142, 531
Field, G. B., Goldsmith, D. W., & Habing, H. J. 1969, ApJ, 155, L149
Fixsen, D. J., Dwek, E., Mather, J. C., Bennett, C. L., & Shafer, R. A. 1998, ApJ, 508, 123
Fong, R., Jones, L. R., Shanks, T., Stevenson, P. R. F., & Strong, A. W. 1987, MNRAS, 224, 1059
Fox, A. J., Savage, B. D., & Wakker, B. P. 2006, ApJS, 165, 229
Gaensler, B. M., Madsen, G. J., Chatterjee, S., & Mao, S. A. 2008, PASA, 25, 184
Gillmon, K., Shull, J. M., Tumlinson, J., & Danforth, C. 2006, ApJ, 636, 891
Górski, K. M., Hivon, E., Banday, A. J., et al. 2005, ApJ, 622, 759
Heiles, C., & Troland, T. H. 2003, ApJ, 586, 1067
Herbstmeier, U., Heithausen, A., & Mebold, U. 1993, A&A, 272, 514
Houck, J. C., & Bregman, J. N. 1990, ApJ, 352, 506
Ingalls, J. G., Miville-Deschênes, M., Reach, W. T., et al. 2004, ApJS, 154, 281
Joncas, G., Boulanger, F., & Dewdney, P. E. 1992, ApJ, 397, 165
Jones, M. H., Rowan-Robinson, M., Branduardi-Raymont, G., et al. 1995, MNRAS, 277, 1587
Kuntz, K. D., & Danly, L. 1996, ApJ, 457, 703
Lagache, G., Haffner, L. M., Reynolds, R. J., & Tufte, S. L. 2000, A&A, 354, 247
Lagache, G., Bavouzet, N., Fernandez-Conde, N., et al. 2007, ApJ, 665, L89
Lamarre, J., Puget, J., Ade, P. A. R., et al. 2010, A&A, 520, A9
Lockman, F. J., & Condon, J. J. 2005, AJ, 129, 1968
Low, F. J., Young, E., Beintema, D. A., et al. 1984, ApJ, 278, L19
Lu, L., Sargent, W. L. W., Savage, B. D., et al. 1998, AJ, 115, 162
Mandolesi, N., Bersanelli, M., Butler, R. C., et al. 2010, A&A, 520, A3
Martin, P. G., Rogers, C., Reach, W. T., Dewdney, P. E., & Heiles, C. E. 1994, in The First Symposium on the Infrared Cirrus and Diffuse Interstellar Clouds, ed. R. M. C. W. B. Latter, ASP Conf. Ser., 58, 188
Martin, P. G., Miville-Deschênes, M., Roy, A., et al. 2010, A&A, 518, L105
Mathis, J. S., Mezger, P. G., & Panagia, N. 1983, A&A, 128, 212
Mennella, A., Butler, R. C., Curto, A., et al. 2011, A&A, 536, A3
Miville-Deschênes, M., & Lagache, G. 2005, ApJS, 157, 302
Miville-Deschênes, M., Boulanger, F., Joncas, G., & Falgarone, E. 2002a, A&A, 381, 209
Miville-Deschênes, M., Lagache, G., & Puget, J. 2002b, A&A, 393, 749
Miville-Deschênes, M., Boulanger, F., Reach, W. T., & Noriega-Crespo, A. 2005, ApJ, 631, L57
Miville-Deschênes, M., Lagache, G., Boulanger, F., & Puget, J. 2007, A&A, 469, 595
Miville-Deschênes, M., Martin, P. G., Abergel, A., et al. 2010, A&A, 518, L104
Planck Collaboration 2011a, A&A, 536, A1
Planck Collaboration 2011b, A&A, 536, A2
Planck Collaboration 2011c, A&A, 536, A7
Planck Collaboration 2011d, A&A, 536, A8
Planck Collaboration 2011e, A&A, 536, A9
Planck Collaboration 2011f, A&A, 536, A10
Planck Collaboration 2011g, A&A, 536, A11
Planck Collaboration 2011h, A&A, 536, A12
Planck Collaboration 2011i, A&A, 536, A13
Planck Collaboration 2011j, A&A, 536, A14
Planck Collaboration 2011k, A&A, 536, A15
Planck Collaboration 2011l, A&A, 536, A16

Planck Collaboration 2011m, A&A, 536, A17
Planck Collaboration 2011n, A&A, 536, A18
Planck Collaboration 2011o, A&A, 536, A19
Planck Collaboration 2011p, A&A, 536, A20
Planck Collaboration 2011q, A&A, 536, A21
Planck Collaboration 2011r, A&A, 536, A22
Planck Collaboration 2011s, A&A, 536, A23
Planck Collaboration 2011t, A&A, 536, A24
Planck Collaboration 2011u, A&A, 536, A25
Planck Collaboration 2011v, The Explanatory Supplement to the Planck Early Release Compact Source Catalogue (ESA)
Planck Collaboration 2011w, A&A, 536, A26
Planck HFI Core Team 2011a, A&A, 536, A4
Planck HFI Core Team 2011b, A&A, 536, A6
Press, W. H., Teukolsky, S. A., Vetterling, W. T., & Flannery, B. P. 1995, Numerical Recipes in C (Cambridge University Press), 994
Rachford, B. L., Snow, T. P., Tumlinson, J., et al. 2002, ApJ, 577, 221
Rachford, B. L., Snow, T. P., Destree, J. D., et al. 2009, ApJS, 180, 125
Reach, W. T., Koo, B., & Heiles, C. 1994, ApJ, 429, 672
Reach, W. T., Wall, W. F., & Odegard, N. 1998, ApJ, 507, 507
Reynolds, R. J. 1989, ApJ, 339, L29
Richter, P., Sembach, K. R., Wakker, B. P., et al. 2001, ApJ, 559, 318
Savage, B. D., & Sembach, K. R. 1996, ARA&A, 34, 279
Savage, B. D., Bohlin, R. C., Drake, J. F., & Budich, W. 1977, ApJ, 216, 291
Sembach, K. R., Wakker, B. P., Tripp, T. M., et al. 2004, ApJS, 150, 387
Shapiro, P. R., & Field, G. B. 1976, ApJ, 205, 762
Shetty, R., Kauffmann, J., Schnee, S., Goodman, A. A., & Ercolano, B. 2009, ApJ, 696, 2234
Spitzer, Jr., L. 1956, ApJ, 124, 20
Stepnik, B., Abergel, A., Bernard, J., et al. 2003, A&A, 398, 551
Tauber, J. A., Mandolesi, N., Puget, J., et al. 2010, A&A, 520, A1
Trifalenkov, I. A. 1993, Astron. Rep., 37, 327
Tripp, T. M., Wakker, B. P., Jenkins, E. B., et al. 2003, AJ, 125, 3122
van Woerden, H., & Wakker, B. P. 2004, in High Velocity Clouds, ed. H. van Woerden, B. P. Wakker, U. J. Schwarz, & K. S. de Boer, 312, 195
Veneziani, M., Ade, P. A. R., Bock, J. J., et al. 2010, ApJ, 713, 959
Wakker, B. P. 2001, ApJS, 136, 463
Wakker, B. P. 2006, ApJS, 163, 282
Wakker, B. P., & Boulanger, F. 1986, A&A, 170, 84
Wakker, B. P., Howk, J. C., Savage, B. D., et al. 1999, Nature, 402, 388
Wheelock, S., Gautier, T. N., Chillemi, J., et al. 1993, ISSA Explanatory Suppl., Tech. Rep.
Witt, A. N., Gold, B., Barnes, F. S., et al. 2010, ApJ, 724, 1551
Zacchei, A., Maino, D., Baccigalupi, C., et al. 2011, A&A, 536, A5

[1] Aalto University Metsähovi Radio Observatory, Metsähovintie 114, 02540 Kylmälä, Finland
[2] Agenzia Spaziale Italiana Science Data Center, c/o ESRIN, via Galileo Galilei, Frascati, Italy
[3] Astroparticule et Cosmologie, CNRS UMR7164, Université Denis Diderot Paris 7, Bâtiment Condorcet, 10 rue A. Domon et Léonie Duquet, Paris, France
[4] Astrophysics Group, Cavendish Laboratory, University of Cambridge, J J Thomson Avenue, Cambridge CB3 0HE, UK
[5] Atacama Large Millimeter/submillimeter Array, ALMA Santiago Central Offices, Alonso de Cordova 3107, Vitacura, Casilla 763 0355, Santiago, Chile
[6] CITA, University of Toronto, 60 St. George St., Toronto, ON M5S 3H8, Canada
[7] CNRS, IRAP, 9 Av. colonel Roche, BP 44346, 31028 Toulouse Cedex 4, France
[8] California Institute of Technology, Pasadena, California, USA
[9] DAMTP, University of Cambridge, Centre for Mathematical Sciences, Wilberforce Road, Cambridge CB3 0WA, UK
[10] DSM/Irfu/SPP, CEA-Saclay, 91191 Gif-sur-Yvette Cedex, France
[11] DTU Space, National Space Institute, Juliane Mariesvej 30, Copenhagen, Denmark
[12] Département de physique, de génie physique et d'optique, Université Laval, Québec, Canada
[13] Departamento de Física, Universidad de Oviedo, Avda. Calvo Sotelo s/n, Oviedo, Spain
[14] Department of Astronomy and Astrophysics, University of Toronto, 50 Saint George Street, Toronto, Ontario, Canada
[15] Department of Physics & Astronomy, University of British Columbia, 6224 Agricultural Road, Vancouver, British Columbia, Canada
[16] Department of Physics, Gustaf Hällströmin katu 2a, University of Helsinki, Helsinki, Finland
[17] Department of Physics, Princeton University, Princeton, New Jersey, USA
[18] Department of Physics, Purdue University, 525 Northwestern Avenue, West Lafayette, Indiana, USA
[19] Department of Physics, University of California, Berkeley, California, USA
[20] Department of Physics, University of California, One Shields Avenue, Davis, California, USA
[21] Department of Physics, University of California, Santa Barbara, California, USA
[22] Department of Physics, University of Illinois at Urbana-Champaign, 1110 West Green Street, Urbana, Illinois, USA
[23] Dipartimento di Fisica G. Galilei, Università degli Studi di Padova, Via Marzolo 8, 35131 Padova, Italy
[24] Dipartimento di Fisica, Università La Sapienza, P.le A. Moro 2, Roma, Italy
[25] Dipartimento di Fisica, Università degli Studi di Milano, Via Celoria 16, Milano, Italy
[26] Dipartimento di Fisica, Università degli Studi di Trieste, Via A. Valerio 2, Trieste, Italy
[27] Dipartimento di Fisica, Università di Ferrara, Via Saragat 1, 44122 Ferrara, Italy
[28] Dipartimento di Fisica, Università di Roma Tor Vergata, Via della Ricerca Scientifica 1, Roma, Italy
[29] Discovery Center, Niels Bohr Institute, Blegdamsvej 17, Copenhagen, Denmark
[30] Dpto. Astrofísica, Universidad de La Laguna (ULL), 38206 La Laguna, Tenerife, Spain
[31] European Southern Observatory, ESO Vitacura, Alonso de Cordova 3107, Vitacura, Casilla 19001, Santiago, Chile
[32] European Space Agency, ESAC, Planck Science Office, Camino bajo del Castillo s/n, Urbanización Villafranca del Castillo, Villanueva de la Cañada, Madrid, Spain
[33] European Space Agency, ESTEC, Keplerlaan 1, 2201 AZ Noordwijk, The Netherlands
[34] Helsinki Institute of Physics, Gustaf Hällströmin katu 2, University of Helsinki, Helsinki, Finland
[35] INAF - Osservatorio Astrofisico di Catania, Via S. Sofia 78, Catania, Italy
[36] INAF - Osservatorio Astronomico di Padova, Vicolo dell'Osservatorio 5, Padova, Italy
[37] INAF - Osservatorio Astronomico di Roma, Via di Frascati 33, Monte Porzio Catone, Italy
[38] INAF - Osservatorio Astronomico di Trieste, Via GB Tiepolo 11, Trieste, Italy
[39] INAF/IASF Bologna, Via Gobetti 101, Bologna, Italy
[40] INAF/IASF Milano, Via E. Bassini 15, Milano, Italy
[41] INRIA, Laboratoire de Recherche en Informatique, Université Paris-Sud 11, Bâtiment 490, 91405 Orsay Cedex, France
[42] IPAG: Institut de Planétologie et d'Astrophysique de Grenoble, Université Joseph Fourier, Grenoble 1 / CNRS-INSU, UMR 5274, 38041 Grenoble, France
[43] Imperial College London, Astrophysics group, Blackett Laboratory, Prince Consort Road, London SW7 2AZ, UK
[44] Infrared Processing and Analysis Center, California Institute of Technology, Pasadena, CA 91125, USA
[45] Institut Néel, CNRS, Université Joseph Fourier Grenoble I, 25 rue des Martyrs, Grenoble, France
[46] Institut d'Astrophysique Spatiale, CNRS UMR8617 Université Paris-Sud 11, Bâtiment 121, Orsay, France
[47] Institut d'Astrophysique de Paris, CNRS UMR7095, Université Pierre & Marie Curie, 98bis boulevard Arago, Paris, France
[48] Institute of Astronomy and Astrophysics, Academia Sinica, Taipei, Taiwan

[49] Institute of Astronomy, University of Cambridge, Madingley Road, Cambridge CB3 0HA, UK
[50] Institute of Theoretical Astrophysics, University of Oslo, Blindern, Oslo, Norway
[51] Instituto de Astrofísica de Canarias, C/Vía Láctea s/n, La Laguna, Tenerife, Spain
[52] Instituto de Física de Cantabria (CSIC-Universidad de Cantabria), Avda. de los Castros s/n, Santander, Spain
[53] Jet Propulsion Laboratory, California Institute of Technology, 4800 Oak Grove Drive, Pasadena, California, USA
[54] Jodrell Bank Centre for Astrophysics, Alan Turing Building, School of Physics and Astronomy, The University of Manchester, Oxford Road, Manchester M13 9PL, UK
[55] Kavli Institute for Cosmology Cambridge, Madingley Road, Cambridge CB3 0HA, UK
[56] LERMA, CNRS, Observatoire de Paris, 61 avenue de l'Observatoire, Paris, France
[57] Laboratoire AIM, IRFU/Service d'Astrophysique - CEA/DSM - CNRS - Université Paris Diderot, Bât. 709, CEA-Saclay, 91191 Gif-sur-Yvette Cedex, France
[58] Laboratoire Traitement et Communication de l'Information, CNRS UMR 5141 and Télécom ParisTech, 46 rue Barrault, 75634 Paris Cedex 13, France
[59] Laboratoire de Physique Subatomique et de Cosmologie, CNRS/IN2P3, Université Joseph Fourier Grenoble I, Institut National Polytechnique de Grenoble, 53 rue des Martyrs, 38026 Grenoble cedex, France
[60] Laboratoire de l'Accélérateur Linéaire, Université Paris-Sud 11, CNRS/IN2P3, Orsay, France
[61] Lawrence Berkeley National Laboratory, Berkeley, California, USA
[62] Max-Planck-Institut für Astrophysik, Karl-Schwarzschild-Str. 1, 85741 Garching, Germany
[63] MilliLab, VTT Technical Research Centre of Finland, Tietotie 3, Espoo, Finland
[64] NRAO, PO Box 2, Rt 28/92, Green Bank, WV 24944-0002, USA
[65] National University of Ireland, Department of Experimental Physics, Maynooth, Co. Kildare, Ireland
[66] Niels Bohr Institute, Blegdamsvej 17, Copenhagen, Denmark
[67] Observational Cosmology, Mail Stop 367-17, California Institute of Technology, Pasadena, CA, 91125, USA
[68] Optical Science Laboratory, University College London, Gower Street, London, UK
[69] SISSA, Astrophysics Sector, Via Bonomea 265, 34136 Trieste, Italy
[70] SUPA, Institute for Astronomy, University of Edinburgh, Royal Observatory, Blackford Hill, Edinburgh EH9 3HJ, UK
[71] School of Physics and Astronomy, Cardiff University, Queens Buildings, The Parade, Cardiff CF24 3AA, UK
[72] Space Sciences Laboratory, University of California, Berkeley, California, USA
[73] Spitzer Science Center, 1200 E. California Blvd., Pasadena, California, USA
[74] Stanford University, Dept of Physics, Varian Physics Bldg, 382 Via Pueblo Mall, Stanford, California, USA
[75] Université de Toulouse, UPS-OMP, IRAP, 31028 Toulouse Cedex 4, France
[76] Universities Space Research Association, Stratospheric Observatory for Infrared Astronomy, MS 211-3, Moffett Field, CA 94035, USA
[77] University of Granada, Departamento de Física Teórica y del Cosmos, Facultad de Ciencias, Granada, Spain
[78] University of Miami, Knight Physics Building, 1320 Campo Sano Dr., Coral Gables, Florida, USA
[79] Warsaw University Observatory, Aleje Ujazdowskie 4, 00-478 Warszawa, Poland